proliferating cell nuclear antigen (PCNA) is loaded by the replication factor C (RFC) clamp loader complex at the double-strand/single-strand DNA template-primer terminus in an ATP-dependent manner (Majka and Burgers, 2004). Subsequent to PCNA loading, the replicative DNA polymerase can access the replication site through an interaction with PCNA. A similar molecular mechanism has been assumed for NER repair synthesis as the gap remaining after damage incision and removal by XP proteins leaves a free 3′-OH terminus with an intact template, which is structurally similar to the replication elongation intermediate (Gillet and Scharer, 2006). In contrast, translesion synthesis (TLS), the bypass of DNA lesions that block replication by normal replicative DNA polymerases, involves a polymerase switch from the replicative to a specialized DNA polymerase (Friedberg et al., 2005a). Ubiquitination of PCNA, which is dependent on the E3 ubiquitin ligase RAD18, facilitates this process (Moldovan et al., 2007). All Y family polymerases have both PCNA-binding and ubiquitin-binding motifs, so ubiquitination of PCNA increases its affinity for these polymerases, thereby mediating the polymerase switch (Bienko et al., 2005; Kannouche et al., 2004; Plosky et al., 2006; Watanabe et al., 2004).

Clamp loaders are heteropentamers comprising four small subunits, RFC2–5, common to all clamp loaders and a large subunit that varies between complexes (Majka and Burgers, 2004). The classical RFC1–5 pentamer loads PCNA onto the DNA during replication. Because of their ability to interact with DNA polymerases, RFC complexes have been often implicated in loading different DNA polymerases themselves as well as loading PCNA and the alternative sliding clamp 9-1-1 (Kai and Wang, 2003; Masuda et al., 2007; Shiomi et al., 2007). The polκ homolog in *S. pombe*, DinB, is reported to be recruited to the replication fork by the 9-1-1 checkpoint clamp and RAD17 clamp loader complex, when the replication machinery encounters DNA damage (Kai and Wang, 2003).

Here we describe roles of three DNA polymerases, polδ, polε, and polκ, which we show are responsible for human NER repair synthesis in vivo. siRNA depletion of these polymerases diminished the repair synthesis activity in vivo. Recruitment of these polymerases into NER repair sites is differentially regulated by the status of PCNA ubiquitination as well as by usage of distinct clamp loader complexes or the repair scaffolding protein XRCC1. Based on the above findings, we propose a model for the involvement of mutagenic and conventional DNA polymerases and their differential loading mechanisms in NER repair synthesis.

RESULTS

UV Damage Induces PCNA Ubiquitination in Quiescent Human Cells

In previous work we and many other groups have highlighted the importance of PCNA ubiquitination in the regulation of TLS during replication of damaged DNA (Lehmann et al., 2007). TLS usually uses Y family DNA polymerases (Ohmori et al., 2001), which are recruited to ubiquitinated PCNA because they have binding motifs for both PCNA (PIP box) and ubiquitin (UBZ motif) (Bienko et al., 2005). We were interested to discover if ubiquitinated PCNA might have functions outside of S phase, so we examined primary human fibroblasts that were maintained for several days in low serum to bring them into quiescence. Figure 1A shows that UV irradiation did indeed result in PCNA ubiquitination in normal (48BR) cells (lanes 2–4), albeit at much lower levels than in exponentially growing SV40-transformed MRC5V1 cells (lane 1). Remarkably, a similar induction of PCNA ubiquitination was observed in XP-A (Figure 1A, lanes 5–7) and XP-C cells (lanes 8–10), indicating that, although UV dependent, it was independent of incision during NER. In all cases, the ubiquitinated PCNA was resistant to extraction by Triton X-100, indicating that it was bound to chromatin (Figure 1B).

The number of S phase cells in these cultures was negligible, as measured by the expression of cycling marker ki67 and nucleoside incorporation (Supplemental Experimental Procedures, available online), so there could be no involvement in replication-associated processes. Furthermore, hydroxyurea treatment for up to 4 hr, which stalls cells in S phase, did not elicit the ubiquitination of PCNA in quiescent normal (Figure 1C, lanes 4 and 5) or XP (lanes 8 and 9 for XP-A and lanes 12 and 13 for XP-C) cells, though it did, as shown previously, induce PCNA ubiquitination in cycling populations in S phase (lane 2) (Bienko et al., 2005).

Ubiquitinated PCNA Is Associated with Proteins Involved in the Late Step of NER

Although the results of Figure 1A indicate that PCNA ubiquitination was not dependent on damage incision during NER, we were interested to discover if it might nevertheless play a role in later steps of NER. In previous work, we have used chromatin immunoprecipitation (ChIP) to identify protein complexes involved in different stages of NER (Fousteri et al., 2006; Moser et al., 2007). In particular we were able to identify a complex that was UV dependent and contained proteins involved in the late, postincision steps of NER, including RPA, XRCC1, and PCNA. Figures 1D and 1E show immunoblots revealing some of the components of this complex following ChIP with anti-PCNA antibody from normal cells under various different conditions. Remarkably, a band corresponding to ubiquitinated PCNA was easily observable in these ChIPs. This band was dependent on UV irradiation and could be observed both in serum-starved (G0) cells (Figures 1D and 1E, lanes 1 and 2) and cycling cells close to confluence (lanes 3 and 4). This represents a considerable enrichment of the ubiquitinated PCNA relative to unmodified PCNA (compare relative intensities of modified and unmodified bands in Figures 1D, 1E, and 1A). We noted in these complexes the presence of polδ both in G0 cells and in cycling cells (Figure 1D), consistent with our previous observations (Moser et al., 2007), and also polε only in cycling cells (Figure 1E). Both of these DNA polymerases have been previously implicated in NER repair synthesis in an in vitro reconstituted system (Araujo et al., 2000). Polη, which is involved in TLS of cyclobutane pyrimidine dimers, was barely detectable in the ChIP (Figure 1E, lane 4). Importantly, the complex also contained polκ (Figure 1D), which we have previously shown to be involved in NER in mouse embryonic fibroblasts (Ogi and Lehmann, 2006). The amount of polκ in the ChIP was significantly higher in G0 cells than in cycling cells (Figures 1D and 1E, compare lanes 2 and 4). The cellular dNTP levels are reduced in quiescent cells, so this finding supports

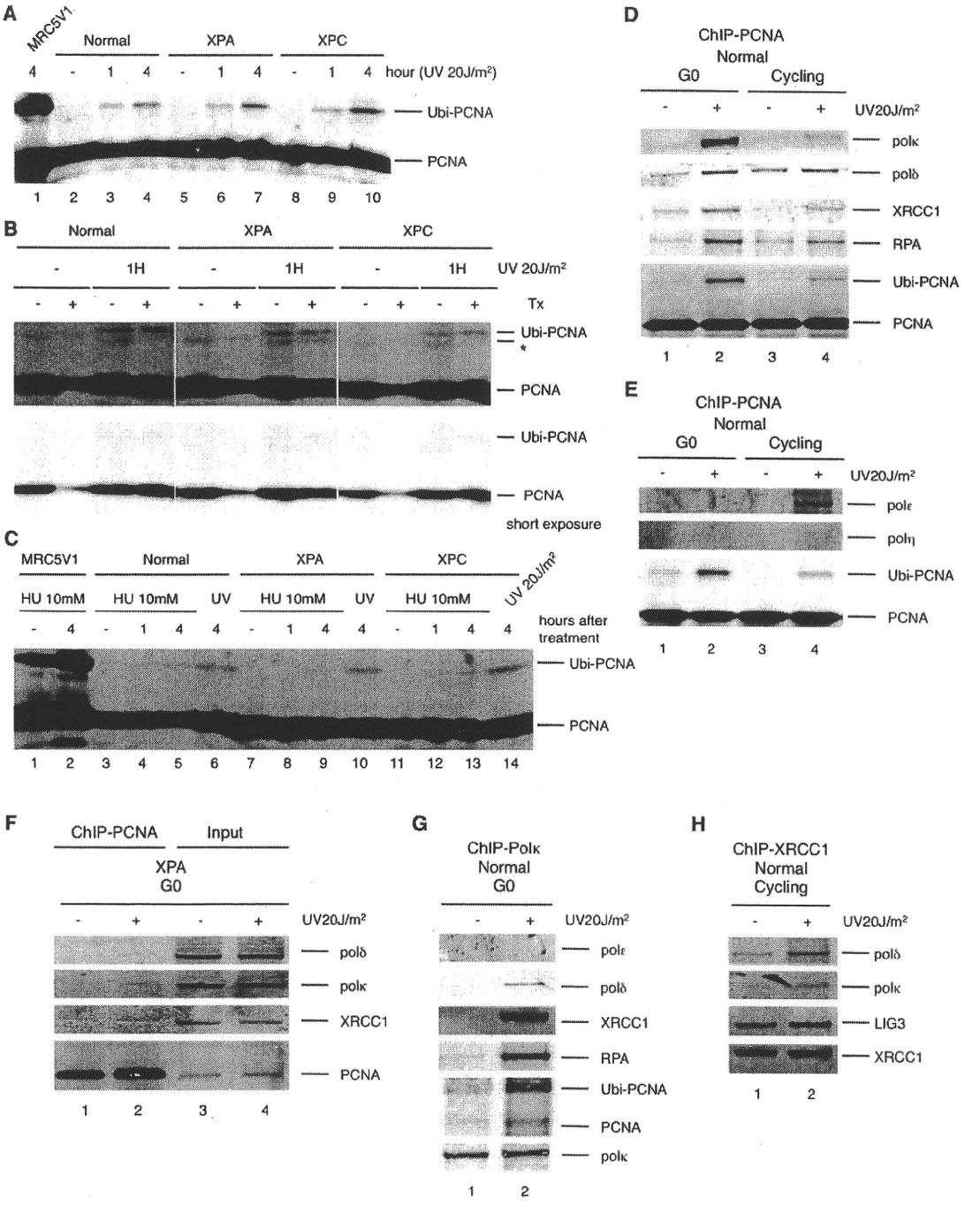

Figure 1. UVC Irradiation-Dependent PCNA Ubiquitination in Quiescent Cells and Interaction of DNA Polymerases with NER Postincision Machinery

(A–C) Western blot showing ubiquitination of PCNA at indicated times after 20 J/m^2 global UVC irradiation (A and B) or 10 mM hydroxyurea (HU) treatment (C) in quiescent cells. Normal (48BR), XPA (XP15BR), and XPC (XP21BR) are all quiescent primary fibroblasts (G0). −, without treatment. SV40-transformed MRC5 cells (MRC5V1) were used as a control. In (B), cells were extracted with Triton X-100 before harvesting (Tx).

(D–H) Normal (VH25) or XPA (XP25RO) primary fibroblasts that were either serum starved (G0) or close to confluent density (Cycling) were globally UVC irradiated (20 J/m^2) and incubated for 1 hr. Repair proteins were then crosslinked to DNA with formaldehyde treatment followed by ChIP with mouse anti-PCNA, PC-10 antibody (D–F), rabbit anti-polκ, K1 antibody (G), or mouse anti-XRCC1, 33-2-5 antibody (H). Coprecipitated proteins were analyzed by western blotting with the antibodies listed in the Supplemental Experimental Procedures. See also Figure S1.

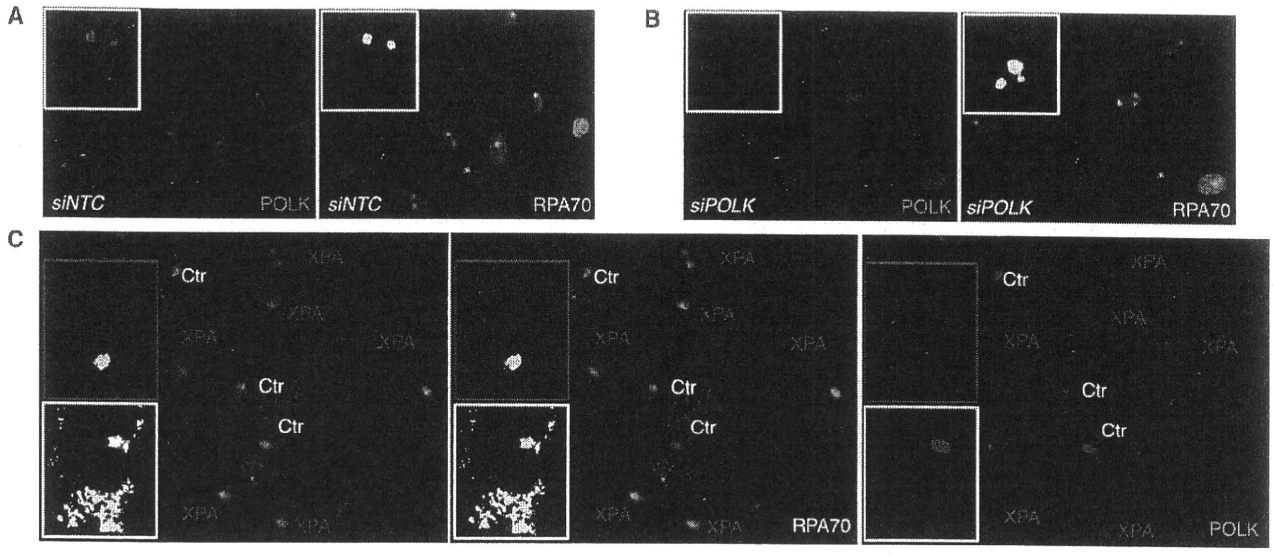

Figure 2. Polκ Accumulation at Local Damage Is Dependent on Early Steps of NER

(A and B) Non-dividing normal 48BR human primary fibroblasts were transfected with either *siNTC* non-targeting control (A) or *POLK* targeting siRNA (B), UVC irradiated (40 J/m^2) through a polycarbonate micropore filter (5 μm), followed by 30 min incubation with 10 mM hydroxyurea and immunostaining with mouse anti-RPA70 (RPA70-9; green) and rabbit anti-polκ (K1; red) antibodies. Blue, DAPI stain.

(C) XP15BR XP-A cells were cocultured with normal 48BR cells containing blue beads (Ctr), UVC irradiated and processed as in (A), except that the post-UVC incubation was for 1 hr without hydroxyurea. The insets in this and subsequent figures show enlarged images of individual cells. The inset in the white box is a normal cell and in the red box an XP cell. See also Figure S2.

our previous proposal that polκ might be the optimal polymerase for NER repair replication when dNTP concentrations are low (Ogi and Lehmann, 2006). Very little of the above proteins were precipitated from unirradiated cells (Figures 1D and 1E, lanes 1 and 3), confirming that these interactions were DNA damage specific. We did not observe any significant interaction in a similar ChIP with anti-PCNA antibody from NER-deficient non-dividing XPA cells (Figure 1F, lanes 1 and 2). Importantly, the same proteins were obtained in the converse experiment using anti-polκ (Figure 1G) as well as anti-XRCC1 (Figure 1H) antibodies for the ChIPs. In particular, Figure 1G shows that polκ and polδ are present in the same repair complex.

Recruitment of DNA Polymerase κ into Repair Sites Is Dependent on NER Damage Incision

To determine if ubiquitinated PCNA is required for recruitment of DNA polymerases to NER complexes, we used the technique of irradiation of non-dividing primary human fibroblasts through a micropore filter to generate damage in localized parts of the nucleus (Volker et al., 2001). We then analyzed the accumulation of polymerases at the sites of local damage (ALD). Using anti-polκ antibodies that detect endogenous levels of polκ (Figures S1A and S1B), we were able to observe polκ ALD following UV irradiation of confluent primary human fibroblasts, where it colocalized with DNA damage (Figure S2A) and with RPA (Figure 2A). Using *POLK* siRNA, we confirmed that these ALD "spots" did indeed represent polκ (Figure 2B and Figure S2B).

Polκ ALD could be observed either in quiescent cells or in cycling cells outside of S phase (Figure S2C), but was not seen in S phase cells (Figure S2D). We previously showed that polκ, unlike the other Y family polymerases, is rarely located in replication factories (Ogi et al., 2005). The intensity of the ALD spots could be amplified by incubation in hydroxyurea after UV irradiation (Figures S2E and S2F, right panels). We have occasionally used hydroxyurea in ALD experiments to obtain clearer images, but in all cases, we have observed similar phenomena with and without the inhibitor, any differences being quantitative rather than qualitative.

We next used XP cells from different complementation groups, whose gene products function in the preincision and dual incision steps of global NER. In XP-A (Figure 2C), -C, and -G cells, and in cells depleted of XPF (Figures S2G–2I), polκ ALD was abolished, whereas it did accumulate at damaged sites in cocultivated normal cells that were loaded with latex beads to distinguish them from the XP cells. Polκ ALD was not affected in Cockayne syndrome (CS-B) cells, which are defective in the transcription-coupled branch of NER (which only contributes to ~5% of the entire NER activity) (Figure S2J). These results show that in human primary fibroblasts, polκ is involved in a late stage of NER that is dependent on successful completion of the early incision steps.

Role of DNA Polymerase κ in NER Repair Synthesis Is Dependent on Its UBZ Zn Finger Domain and PCNA Ubiquitination by *RAD18*

We next examined if recruitment of polκ during NER was dependent on PCNA ubiquitination. A key enzyme required to ubiquitinate PCNA is the E3 ubiquitin ligase RAD18 (Hoege et al., 2002; Kannouche et al., 2004; Watanabe et al., 2004). In a previous report, RAD18 was shown to regulate polκ recruitment to stalled

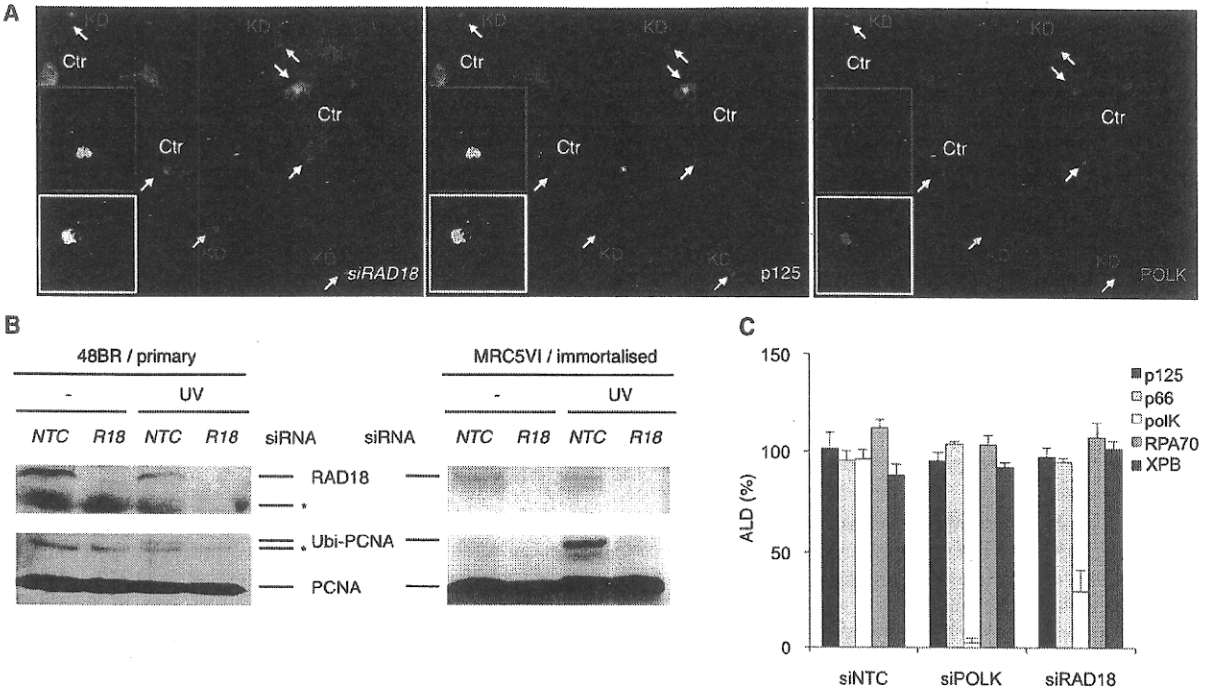
A
Ctr
KD
siRAD18
p125
POLK
B
48BR / primary
MRC5VI / immortalised
UV
NTC
R18
siRNA
RAD18
Ubi-PCNA
PCNA
C
ALD (%)
150
100
50
0
p125
p66
polK
RPA70
XPB
siNTC
siPOLK
siRAD18
D
wtPOLK
D644A
D799A
D644A / D799A
C779A / C782A
Merge
GFP-POLK
RPA
E
Average nuclear intensity (AU)
8
4
0
siNTC
siPOLK
siRAD18
siPOLK/ RAD18

replication forks during TLS of bulky DNA adducts (Bi et al., 2006). We therefore examined the effect of depleting RAD18 on ALD of polκ in NER repair synthesis. In these experiments, we cocultivated cells treated with a non-targeting control and loaded with latex beads with cells treated with a specific *RAD18* siRNA. Depletion of RAD18 resulted in a reduction in polκ ALD (Figure 3A, right panel, compare nuclei indicated with green [polκ ALD negative] and white [polκ ALD positive] arrows); we also confirmed that PCNA ubiquitination after UVC irradiation was completely abolished in the cells treated with *RAD18* siRNA (Figure 3B). The ALD data are quantitated in Figure 3C.

Polκ contains two C2HC ubiquitin-binding zinc finger (UBZ) motifs that are required for binding of polκ to ubiquitinated PCNA (Bienko et al., 2005; Guo et al., 2008). Apart from the cysteine residues, D644 and D799 are crucial aspartate residues that are essential for binding of the zinc finger to ubiquitin (Bienko et al., 2005). We mutated different residues in one or both of these motifs and found that this abolished polκ ALD (Figure 3D). (Figure S2K shows expression levels of the different GFP-polκ constructs. These varied about twofold between cells expressing different constructs, but there was no correlation between expression level and ALD.)

ALD and ChIP measure the recruitment of proteins to the sites of DNA damage but do not prove unequivocally that they are required for repair of the damage. We therefore measured the repair replication step of NER, using a recently developed fluorescence-based variation of the unscheduled DNA repair synthesis (UDS) assay by incorporation of a thymidine analog, ethynyl deoxyuridine (Figures S3A and S3B) (Limsirichaikul et al., 2009). As shown in Figure 3E and Figure S3C, depleting cells of polκ yielded a substantial reduction in UDS, similar to the reduction that we previously observed in *Polk*-deficient mouse embryonic fibroblasts (Ogi and Lehmann, 2006). Depletion of RAD18 resulted in a comparable level of reduction in UDS and depletion of both RAD18 and polκ resulted in only a slight further reduction. To rule out any off-target effects from these pools of four siRNAs, we also analyzed the effects of each siRNA individually. Figure S3D shows that each individual siRNA had a similar effect to the pool, ruling out any off-target effects. Taken together, the data of Figures 1–3 suggest that polκ is recruited to sites of NER by binding to ubiquitinated PCNA, where it is involved in repair synthesis at about 50% of the repair sites.

Polymerase δ and NER

Mammalian polδ contains four subunits, p125, p66, p50, and p12 (Podust et al., 2002). p125 and p50 are the catalytic-core subunits (Lee et al., 1991) and p66 is an accessory factor that binds to PCNA (Hughes et al., 1999). Confirming our previous results (Moser et al., 2007), polδ accumulates at local damage, as shown for both p125 and p66 in Figure 3A (middle for p125) and Figure 4A (top for p125 and middle for p66). In contrast to polκ, ALDs of p125 and p66 were unaffected by depletion of RAD18 (compare green and white arrows in Figure 3A; quantitation in Figure 3C), suggesting that ubiquitination of PCNA is not required for recruitment of polδ to NER sites following incision by the XP proteins.

We next investigated the interdependency of polκ and polδ for relocation to DNA damage. We anticipated that the localization of polκ might be dependent on the p66 subunit of polδ as p66 has been implicated in recruiting translesion polymerases to stalled replication forks in yeast (Gerik et al., 1998; Gibbs et al., 2005). Additionally, the contribution of p66 to recruiting the polδ catalytic core to PCNA loaded onto DNA is still contentious: Pol32p, the p66 subunit of yeast polδ, is dispensable for cell viability, suggesting that it is not essential for DNA synthesis itself (Gerik et al., 1998). Some in vitro evidence also suggests that DNA synthesis activity of polδ stimulated by PCNA may not be strongly dependent on p66 (Podust et al., 2002; Zhou et al., 1997), although contradictory data have also been reported (Ducoux et al., 2001; Masuda et al., 2007; Shikata et al., 2001). To determine the roles of p66 in NER repair synthesis, we examined the effects of siRNA depletion of *POLD3* (p66) as well as *POLD1* (p125) on ALD of the polymerases. Interestingly, ALD of polδ p125 catalytic core was dependent on the p66 subunit (Figure 4A, top right; and Figure 4B), whereas ALD of the p66 subunit was independent of p125 (middle center panel); this observation favors the previous reports suggesting that p66 is crucial for DNA synthesis (Ducoux et al., 2001; Masuda et al., 2007; Shikata et al., 2001). ALD of polκ was not dependent on either subunit of polδ (Figure 4A, bottom); in fact, depletion of

Figure 3. Role of Polκ in NER Is Dependent on PCNA Ubiquitination

(A) siRNA knockdown of RAD18 diminishes the ALD of polκ but not polδ. Cells incubated with blue beads and siRNA non-targeting control were cocultivated with cells incubated with *RAD18* siRNA and locally UVC irradiated (5 μm pores, 40 J/m^2), followed by 1 hr incubation without inhibitors. White arrows indicate polδ (p125; green) and polκ (red) double positive nuclei in cells treated with non-targeting control (also in inset in white box), whereas green arrows indicate nuclei with polδ spots only in cells treated with *RAD18* siRNA (also shown in inset in red box).

(B) Western blot showing that siRNA knockdown of RAD18 abolishes PCNA ubiquitination. Normal 48BR primary fibroblasts (left) or normal but SV40 immortalized MRC5VI cells (right) were transfected with either *siNTC* non-targeting control (*NTC*) or *RAD18* targeting (*R18*) siRNA and cultured at close to confluent density. Cells were globally UVC irradiated (10 J/m^2), followed by incubation for 1 hr without inhibitors. RAD18 and the ubiquitinated PCNA were respectively detected by rabbit anti-RAD18 (Abcam) and mouse anti-PCNA (PC-10) antibodies. Asterisks indicate non-specific bands.

(C) ALD of indicated NER proteins in 48BR cells depleted of RAD18 or polκ using siRNAs. Cells were locally UVC irradiated as in (A). Percentage of ALD represents the relative percentage of cells showing ALD of the indicated protein above a predetermined threshold compared with the percentage in relevant controls. Bars and error bars indicate, respectively, averages and standard deviations calculated from at least three independent experiments.

(D) ALD of wild-type or indicated mutants of polκ. SV40-transformed MRC5 cells were transfected with plasmid expressing either GFP-tagged wild-type human *POLK* or *POLK* with UBZ mutations at the indicated amino acid positions (GFP-POLK; green; see also Figure S2K). Cells were locally UVC irradiated as in (A), followed by immunostaining with anti-RPA antibody (RPA70-9; red).

(E) Effect of RAD18 and polκ depletion on UDS. 48BR cells were transfected with indicated siRNAs and UVC irradiated (10 J/m^2) followed by EdU incorporation for 2 hr. Bars and error bars, respectively, indicate averages and standard deviations of nuclear fluorescent intensity measured in at least 250 nuclei from at least five different positions. See also Figure S3.

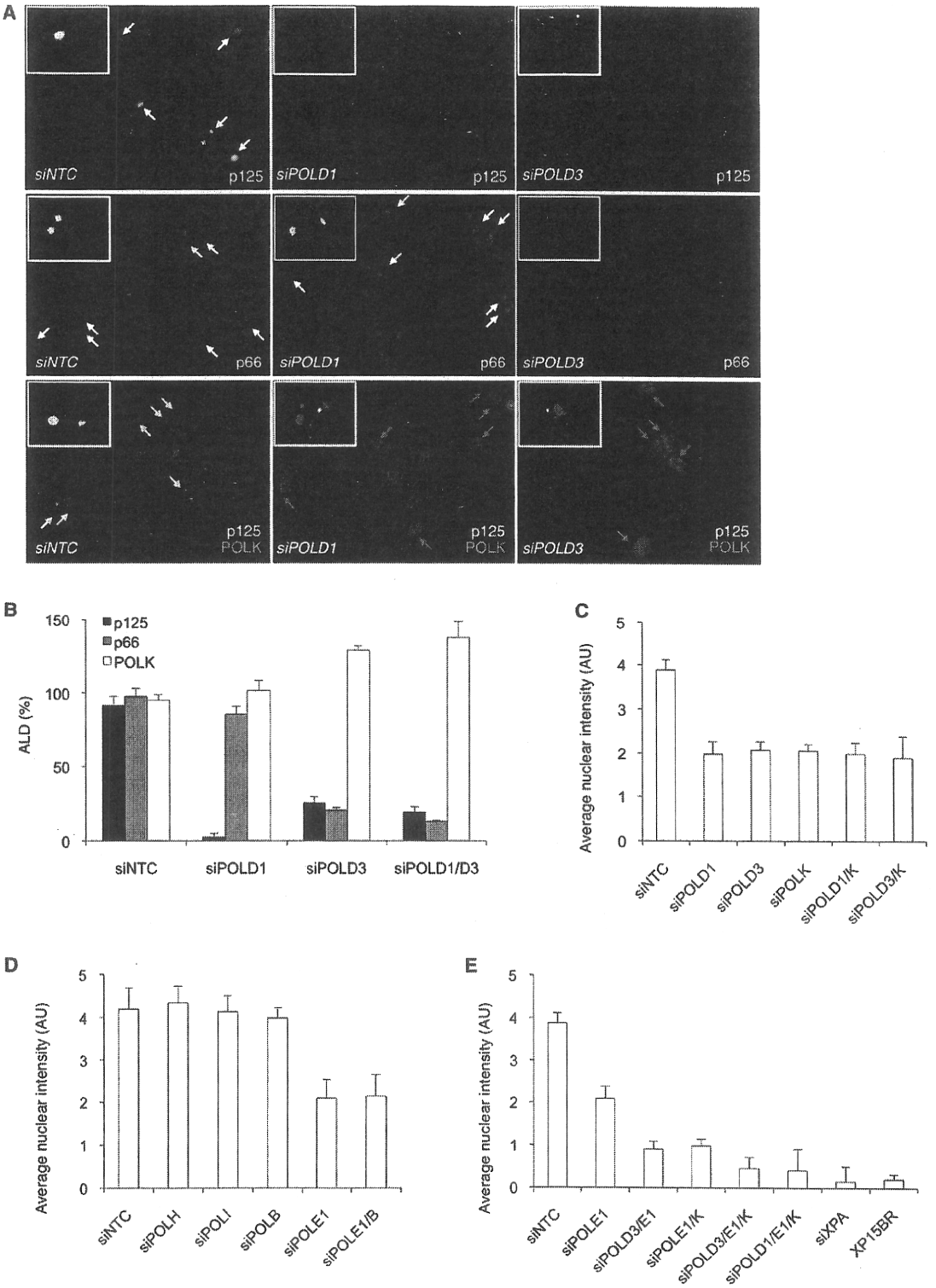

Figure 4. Effects of DNA Polymerase Knockdowns on UDS and ALD

(A) ALD of polδ p125 (A-9 antibody; top and bottom, green), p66 (3E2 antibody; middle, green), and polκ (K1 antibody; bottom, red) in primary 48BR cells treated with the indicated siRNA and locally UVC irradiated (40 J/m^2) followed by 30 min incubation. In the top and middle panels, white arrows represent nuclei with spots of indicated polδ subunit, whereas in the bottom panel, green and red arrows indicate nuclei with polδ p125 and polκ spots, respectively. Note that smaller sized green spots seen in the bottom panels are nonspecific nucleoli staining.

the polδ subunit(s) resulted in a modest increase in polκ ALD (Figure 4B). These data show that polκ and polδ are recruited to damage independently and that recruitment of polδ requires its p66 subunit.

DNA Polymerases δ, ε, and κ, but Neither β, η, nor ι, Are Responsible for NER Repair Synthesis

We next examined the effects of DNA polδ depletion on repair synthesis activity. As shown in Figure 4C (see also Figure S3C), depleting cells of the p125 (*POLD1*) or p66 (*POLD3*) subunits of polδ resulted in a 50% reduction in UDS, as observed with polκ depletion. However depletion of either subunit of polδ together with polκ had no further effect, suggesting that these two polymerases play roles in the same subpathway of repair replication. This conclusion is supported by the finding of both polymerases in the same repair complex, as shown above in Figure 1G. To determine which polymerase might be responsible for the remaining ~50% of UDS when both polκ and/or polδ are depleted, we examined the effects on UDS of depleting other polymerases. Polβ is well known to interact with the XRCC1/Lig3 complex, which we recently showed was involved in the ligation step of NER (Moser et al., 2007); however, in the same report, we failed to demonstrate the recruitment of polβ into NER repair sites (Moser et al., 2007). Consistent with this report, we found that depletion of polβ (*POLB*) had no significant effect on UDS, as was also the case for depletion of the Y family polη or polι (Figure 4D). In striking contrast, depletion of polε reduced UDS by about 50% (Figure 4D). Depletion of polε together with polβ did not elicit any further decrease (Figure 4D), but depletion of both polε and either polδ (*POLD3*) or polκ reduced UDS to about 25% and depletion of all three left only 10%–15% of the level in normal cells (Figure 4E). Since this is also the level that we observed in cells depleted of *XPA*, or a completely NER-defective XP-A cell strain (Figure 4E and Figures S3C and S3D; Limsirichaikul et al., 2009), we regard this as the detection limit of the technique and conclude that polε is indeed responsible for the repair synthesis that is not completed by polδ and polκ. Consistent with this we were able to detect ALD of polε under mild permeabilization conditions (Figure S4A). Whereas ALD of all other proteins was resistant to Triton X-100 extraction, polε that had accumulated at local damage was extracted by the same triton treatment (Figure S4B). This suggests that polε is less tightly bound to chromatin than other proteins or that it is bound more transiently. Taken together, our data show that three polymerases, polδ, polε, and polκ, are responsible for almost the entire repair synthesis in primary human cells.

Differential DNA Polymerase-Loading Mechanisms in NER Repair Synthesis

The above findings prompted us to consider differential polymerase recruitment mechanisms in NER repair synthesis, as the recruitment kinetics as well as the epistatic effects of polymerase depletions on UDS seemed different between polδ/κ and polε.

We first attempted to find out if any other clamps, clamp loaders, and scaffold proteins were required for recruitment of polδ and polκ during NER. We expected that the involvement of (unmodified) PCNA in the recruitment of polδ and of ubiquitinated PCNA in recruitment of polκ would implicate a clamp-loading complex in the recruitment of these polymerases. Although depletion of RFC1, RFC4, or both subunits reduced ALD of polδ-p125, surprisingly it had no effect on ALD of either polκ or polδ-p66 (Figures 5A and 5B). This finding indicates that the recruitment of DNA polymerases may not require post-UV loading of PCNA onto chromatin by the conventional RFC1-RFC. Additionally, RFC-independent p66 recruitment is consistent with a recent publication suggesting that p66 can compete with RFC and prevent pre-loaded PCNA being unloaded or relocated from the 3′ termini of replication sites by RFC (Masuda et al., 2007).

We next examined the effects of depleting either the checkpoint clamp loader RAD17 and also the checkpoint activator ATR. We found no significant effect on ALD of polκ or polδ (Figure 5A), in contrast to a report that the *S. pombe* ortholog of polκ is recruited to stalled replication forks by RAD17 and the 9-1-1 complex (Kai and Wang, 2003). Depletion of two other alternative clamp loader large subunits, CTF18 or FRAG1, had no effect on ALD of polκ, polδ-p66, or polδ-p125 (Figure 5A). In contrast, the scaffold protein XRCC1, previously shown to be a component of the postincision complex (Moser et al., 2007), was needed for ALD of polκ (Figures 5A and 5C). Depletion of any of the factors needed for ALD of polδ or polκ also resulted in a 50% reduction in UDS, whereas depletion of ATR or RAD17 had very little effect on repair synthesis (Figure 5D). In summary, these experiments suggest that polδ-p125 is loaded onto PCNA by RFC1-RFC and p66, whereas polκ is loaded onto ubiquitinated PCNA and requires XRCC1 but not RFC. Failure to load either of these polymerases results in a reduction in UDS to about 50% of its normal level, similar to that found by depleting the polymerases.

We have further examined whether any of the loading factors might also be needed for ALD of polε. As shown in Figure 5E, depletion of RAD18 did not elicit any reduction in polε ALD, suggesting that polε is loaded onto unmodified PCNA. Depletion of XRCC1 or the alternative clamp loader large subunits, RAD17 or FRAG1, did not affect polε ALD; however, depletion of either RFC4 or CTF18 resulted in a reduction in polε ALD, suggesting that CTF18-RFC is involved in loading polε in repair synthesis (Figures 5E and 5F). CTF18 is the human homolog of yeast Ctf18p, which is essential for accurate chromosome transmission, being implicated in sister chromatid cohesion (Hanna et al., 2001) and double strand break repair (Ogiwara et al., 2007). Additionally, recent reports demonstrated that CTF18-RFC can stimulate the activity of polη (Shiomi et al., 2007) as well as polδ (Bermudez

(B) Histogram analyses are shown. Bars and error bars indicate, respectively, averages and standard deviations of the percentages of ALD calculated from at least three independent experiments shown in (A).

(C–E) Effects of multiple DNA polymerase knockdowns on UDS. 48BR cells were transfected with indicated siRNAs and UVC irradiated (10 J/m^2) followed by EdU incorporation for 2 hr. Bars and error bars, respectively, indicate averages and standard deviations of nuclear fluorescent intensity measured in at least 250 nuclei from at least five different positions.

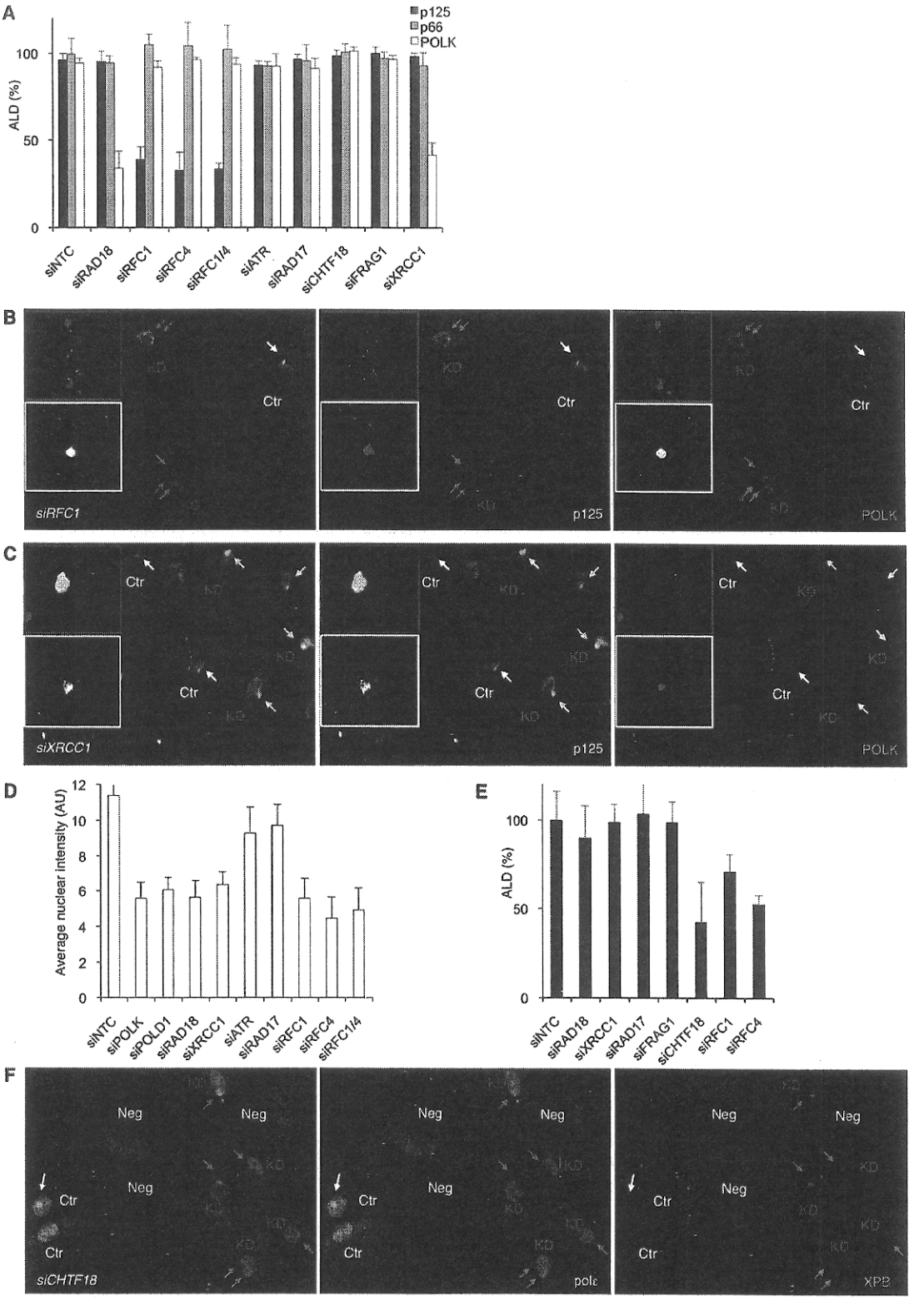

Figure 5. Differential Requirement of Repair Replication Factors for Recruitment of Gap-Filling DNA Polymerases

(A) ALD of polδ p125, p66, and polκ in 48BR cells depleted of indicated genes using siRNAs and local UVC irradiation (40 J/m^2) followed by 1 hr incubation without inhibitors. Bars and error bars indicate, respectively, averages and standard deviations of the percentages of ALD calculated from at least three independent experiments.

et al., 2003), suggesting that CTF18-RFC may play a role in loading specific polymerases during replication when needed.

We also observed a modest reduction of polε ALD in cells depleted of RFC1 (Figure 5E); however, because of the aforementioned technical issue, the experimental errors were substantially larger than errors in ALD measurements of the other proteins.

Considering these polε ALD results together, we propose that loading of polε onto PCNA is mainly dependent on the alternative clamp loader complex CTF18-RFC.

DISCUSSION

Our results have revealed an unexpected complexity in repair synthesis in human cells. Approximately 50% of the repair synthesis used polκ recruited by ubiquitinated PCNA and XRCC1, together with polδ recruited by the classical RFC complex. The remaining 50% is carried out by polε recruited by the CTF18-RFC complex. We propose the following model to explain our findings. RAD18 accumulates at sites of UV damage very rapidly and independently of NER-mediated dual incision (Figure 6A) (Nakajima et al., 2006; unpublished data). Ubiquitination of preloaded PCNA and repositioning of PCNA to the site of the lesion may therefore occur before completion of the preincision complex assembly (Figure 6B). In support of this suggestion, we have been able to detect low levels of ALD of PCNA (but not of polδ) in several NER-deficient XP primary fibroblasts (J. Moser, R.M.O., and M.I.F., unpublished data). Our results delineate two pathways for repair synthesis, following incision, one dependent on polε and the other requiring both polδ and polκ. One possibility is that the former deals with damage on the leading strand and the latter on the lagging strand. We consider, however, a more likely explanation to be that different mechanisms are used to deal with different conformations of the repair sites or of the chromatin structure around the damaged sites. We suggest that 50% of the sites are in an accessible configuration and polε can carry out repair synthesis rapidly (Figures 6Ca–6Ea). In mode 1, polε recruitment by CTF18-RFC occurs following conventional dual incision; possibly, recruitment of polδ and polκ might be inhibited (Figures 6Ca–6Da). After completion of repair synthesis, release of polε and recruitment of LigI occur (Figure 6Ea).

In the second pathway, for example, because of the conformation of the repair site or the chromatin structure, repair synthesis is more difficult, resulting in 3′ incision being delayed relative to 5′ incision (Figure 6Cb). This causes displacement synthesis, as was also proposed in early studies (Mullenders et al., 1985; Smith and Okumoto, 1984) and is consistent with the recent finding that XPF cleaves on the 5′ side of the damage prior to cleavage on the 3′ side by XPG, thereby leaving a 5′ flap to be displaced (Staresincic et al., 2009). This second mode (Figures 6Cb–6Eb) has more rigid requirements because of the surrounding steric hindrance; this mode involves both polδ and polκ. Recruitment of polδ occurs independently of PCNA ubiquitination status, but does depend on its accessory p66 subunit as well as the RFC complex (Figure 6Cb), whereas recruitment of polκ requires XRCC1 as well as ubiquitination of PCNA (Figure 6Db). Hydroxyurea prevents completion of repair synthesis, resulting in an accumulation of repair synthesis intermediates, perhaps because of displacement synthesis as suggested earlier (Mullenders et al., 1985; Smith and Okumoto, 1984), and an increased ALD of repair synthesis proteins.

XRCC1 appears to have a fairly direct, as yet undefined, role in recruiting polκ, and, after completion of repair synthesis, release of polymerases from the repair patch and XRCC1-dependent recruitment of LigIII occur (Figure 6Eb). Our data are consistent with a recent report suggesting that in vitro polδ is rather distributive, even in the presence of PCNA, whereas RFC remains at the primer terminus (Masuda et al., 2007). Which of the polymerases operates first in mode 2 and why both are needed will be the subject of future studies.

The major function of Y family DNA polymerases is believed to be in TLS, the bypass of DNA lesions that block replication by normal replicative DNA polymerases (Prakash et al., 2005). Because of this property, the replication fidelities of the Y family enzymes are very low (McCulloch and Kunkel, 2008). Polκ is specialized for TLS past bulky DNA lesions (Avkin et al., 2004; Ohashi et al., 2000b; Suzuki et al., 2002) and induces mutations when it acts on undamaged templates with a frequency of about 10^{-3} (Ohashi et al., 2000a; Zhang et al., 2000). We have considered the possibility that when there are two closely spaced lesions on opposite strands, repair synthesis on one strand will need to bypass the lesion on the opposite strand and that the role of polκ is to carry out this TLS step. Lam and Reynolds (1986) carried out a detailed analysis of the frequency of closely spaced lesions in human fibroblasts. After a dose of 40 J/m^{-2} used in our ALD experiments, they found that the proportion of overlapping lesions ($0.8/10^8$ daltons) represented only 0.5% of the total lesions ($1.5/10^6$ daltons). We think that this is unlikely to explain our data. There is increasing evidence that apart from their roles in TLS, Y family polymerases have other functions as well

(B) Depletion of RFC1 abolishes polδ ALD but does not affect polκ ALD. Cells with non-targeted siRNA cultured with blue beads were cocultured with cells in which RFC1 was depleted by siRNA. White arrow indicates polδ (p125; green) and polκ (red) double positive nuclei, whereas red arrows indicate nuclei with polκ spots only. KD, knockdown (also inset with red box); Ctr, control (also inset in white box).

(C) Depletion of XRCC1 abolishes polκ ALD but does not affect polδ ALD. White arrows indicate polδ (p125; green) and polκ (red) double positive nuclei, whereas green arrows indicate nuclei with polδ spots only.

(D) UDS following depletion of indicated genes. 48BR cells were transfected with indicated siRNAs and UVC irradiated (10 J/m^2) followed by EdU incorporation for 2 hr. Bars and error bars, respectively, indicate averages and standard deviations of nuclear fluorescent intensity measured in at least 250 nuclei from at least five different positions.

(E) ALD of polε in 48BR cells depleted of indicated genes using siRNAs. Cells were pre-fixed before immunostaining, as described in Figure S4. Bars and error bars indicate, respectively, averages and standard deviations of the percentages of ALD calculated from at least three independent experiments.

(F) Depletion of CTF18 inhibits polε ALD. Cells with non-targeted siRNA cultured with blue beads were cocultured with cells in which CTF18 was depleted by siRNA. As described in Figure S4, cells were pre-fixed before immunostaining. White arrow indicates polε (green) and XPB (red) double positive nuclei, whereas red arrows indicate nuclei with XPB spots only. Neg, polε negative non-cycling cells.

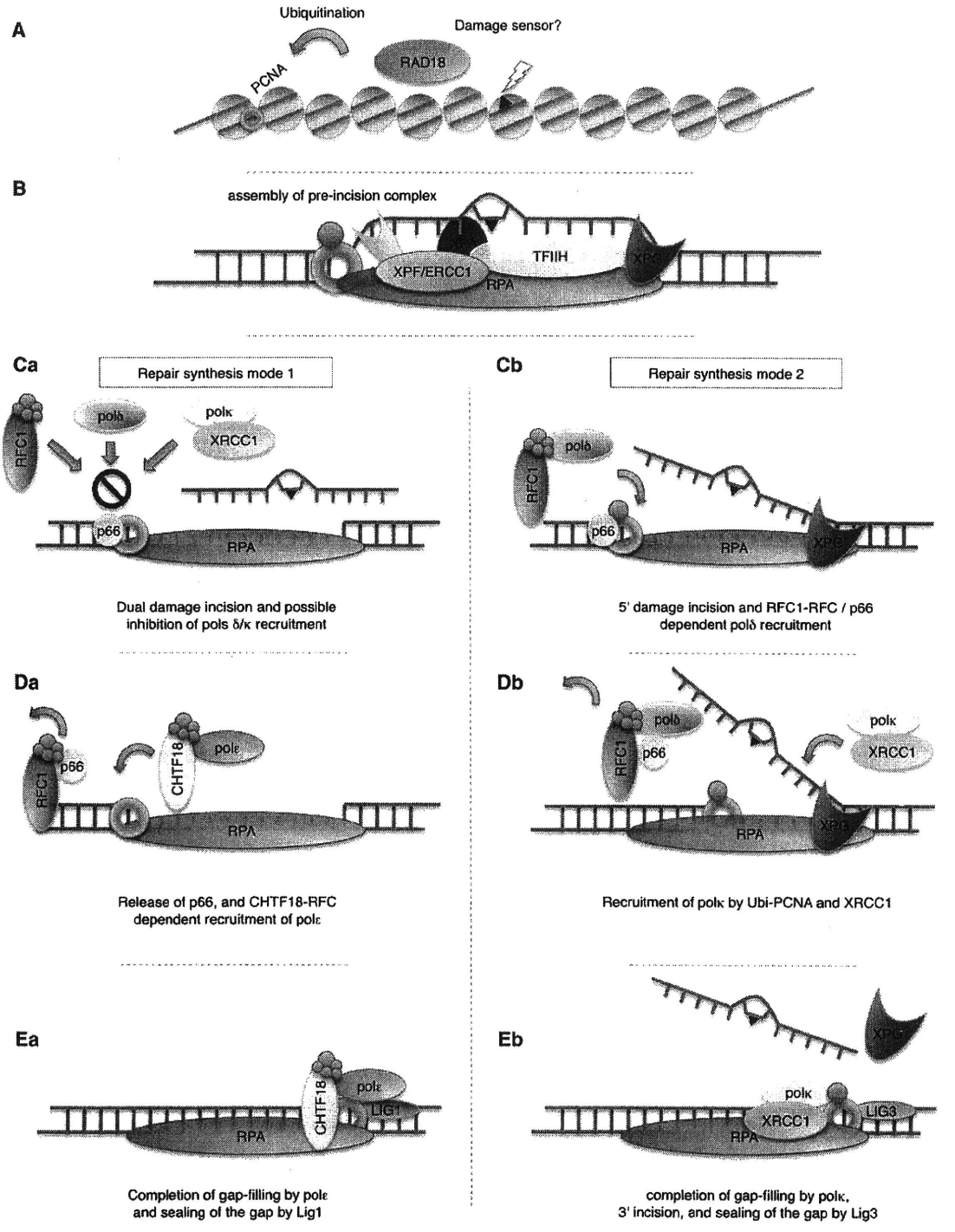

Figure 6. Model for Action of Polκ and Polδ during NER Gap-Filling DNA Synthesis

(A) Section of chromatin in quiescent cells with PCNA loaded on the DNA and damage sensed by RAD18, which is then able to ubiquitinate PCNA.

(B) Assembly of the preincision complex.

(Ca–Ea) In mode 1, following dual incisions to release the damaged fragment (Ca), polε is recruited by CTF18-RFC to fill the gap (Da), followed by Ligase I recruitment to seal the nick (Ea).

(Cb–Eb) In mode 2, 5′ incision is followed by recruitment of both polδ core by RFC and p66 (Cb) and polκ/XRCC1 by ubiquitinated PCNA (D2). (Eb) After completion of repair synthesis, polκ is released, XPG cleaves off the flap, and XRCC1 recruits Ligase III to seal the remaining nick.

(reviewed in Lehmann, 2006). At first sight it may seem strange that the cell uses an error-prone polymerase to carry out NER repair synthesis. However, we have previously speculated that the low K_m of polκ may make it especially suitable for use under conditions of low nucleotide concentration (Ogi and Lehmann, 2006). An error frequency of 10^{-3} together with a patch size of 30 nucleotides would result in about one error every 30 repair patches. This may be a price worth paying for the cell to carry out successful repair synthesis. We speculate that polκ may in this way contribute to UV-induced mutagenesis in normal human cells, especially in quiescence. Indeed, the bacterial homolog of polκ, DinB, is believed to be involved in untargeted mutagenesis in *E. coli*, a mutagenic process that occurs on non-damaged DNA templates—independently of TLS—under conditions of starvation (Brotcorne-Lannoye and Maenhaut-Michel, 1986).

Our results, though raising many new questions, give important insights into the complexity of repair synthesis and the role of different polymerases in this process.

EXPERIMENTAL PROCEDURES

Antibodies and Cell Lines

Antibodies and cell lines used in the study are described in detail in the Supplemental Experimental Procedures.

RNA Interference

All the siRNA oligos were purchased from Dharmacon (the sequences can be obtained from the authors upon request). Cells were transfected using HiPerfect (QIAGEN) according to the manufacturer's instruction. Immunostaining and UDS experiments were performed 48 hr after transfection. Knockdown efficiencies were confirmed by western blot and immunofluorescence.

ChIP Assay

Experimental details have been described previously (Fousteri et al., 2006; Moser et al., 2007). Confluent or serum-starved cells were UVC irradiated (20 J/m^2) and incubated for 1 hr prior to in vivo crosslinking (11 min, on ice) and ChIP. Antibodies used for the ChIP are described in the Supplemental Experimental Procedures.

Local UV Irradiation and Immunofluorescence

Experimental details have been described previously (Volker et al., 2001). Cells were grown on coverslips and locally UVC irradiated (40 J/m^2) through a polycarbonate filter (pore size of 5 μm), followed by incubation for 0.5 to 1 hr. Cells were fixed and stained with antibodies described in detail in Supplemental Experimental Procedures. Photographs were captured with a Zeiss Axioobserver microscope.

Unscheduled DNA Synthesis Assay

Experimental details have been described previously (Limsirichaikul et al., 2009). Cells were siRNA transfected and grown on coverslips before the experiments. Cells were globally UVC irradiated (10 J/m^2) and incubated for 2 hr in medium supplemented with 10 μM EdU. After EdU incorporation, coverslips were processed as described in detail in Supplemental Experimental Procedures. Photographs were captured with a KEYENCE BIOREVO BZ-9000 system.

More detailed and additional experimental procedures are described in the Supplemental Experimental Procedures.

SUPPLEMENTAL INFORMATION

Supplemental Information includes Supplemental Experimental Procedures and four figures and can be found with this article online at doi:10.1016/j.molcel.2010.02.009.

ACKNOWLEDGMENTS

This work was supported by Special Coordination Funds for Promoting Science and Technology from Japan Science and Technology Agency (JST), a Grant in aid for Scientific Research KAKENHI (20810021) from Japan Society for the Promotion of Science, a cancer research grant from the YASUDA Medical Foundation, a research grant from Uehara Memorial Foundation, a medical research grant from Takeda Science Foundation, a Grant in aid for Honeybee Research from Yamada Apiculture Center Inc., a Grant in aid for Seeds Innovation (Type-A) from JST, and a Butterfield Medical Award from the Great Britain Sasakawa Foundation to T.O.; a Global COE Program from the Ministry of Education, Culture, Sports, Sciences and Technology of Japan to T.O., S.L., Y.N., and S.Y.; a KAKENHI to K.T. and Y.M.; a Medical Research Council programme grant to A.R.L.; and an EC-RTN and integrated project to A.R.L. and L.M. We are grateful to Y. Gushiken for anti-polκ antibody purification. The anti-polε antibody, 3A3.2, is a kind gift from S. Linn (University of California, Berkeley).

Received: May 26, 2009
Revised: September 25, 2009
Accepted: December 21, 2009
Published: March 11, 2010

REFERENCES

Aboussekhra, A., Biggerstaff, M., Shivji, M.K., Vilpo, J.A., Moncollin, V., Podust, V.N., Protic, M., Hubscher, U., Egly, J.M., and Wood, R.D. (1995). Mammalian DNA nucleotide excision repair reconstituted with purified protein components. Cell *80*, 859–868.

Andressoo, J.O., and Hoeijmakers, J.H. (2005). Transcription-coupled repair and premature ageing. Mutat. Res. *577*, 179–194.

Araujo, S.J., Tirode, F., Coin, F., Pospiech, H., Syvaoja, J.E., Stucki, M., Hubscher, U., Egly, J.M., and Wood, R.D. (2000). Nucleotide excision repair of DNA with recombinant human proteins: definition of the minimal set of factors, active forms of TFIIH, and modulation by CAK. Genes Dev. *14*, 349–359.

Avkin, S., Goldsmith, M., Velasco-Miguel, S., Geacintov, N., Friedberg, E.C., and Livneh, Z. (2004). Quantitative analysis of translesion DNA synthesis across a benzo[*a*]pyrene-guanine adduct in mammalian cells: the role of DNA polymerase κ. J. Biol. Chem. *279*, 53298–53305.

Bermudez, V.P., Maniwa, Y., Tappin, I., Ozato, K., Yokomori, K., and Hurwitz, J. (2003). The alternative Ctf18-Dcc1-Ctf8-replication factor C complex required for sister chromatid cohesion loads proliferating cell nuclear antigen onto DNA. Proc. Natl. Acad. Sci. USA *100*, 10237–10242.

Bi, X., Barkley, L.R., Slater, D.M., Tateishi, S., Yamaizumi, M., Ohmori, H., and Vaziri, C. (2006). Rad18 regulates DNA polymerase κ and is required for recovery from S-phase checkpoint-mediated arrest. Mol. Cell. Biol. *26*, 3527–3540.

Bienko, M., Green, C.M., Crosetto, N., Rudolf, F., Zapart, G., Coull, B., Kannouche, P., Wider, G., Peter, M., Lehmann, A.R., et al. (2005). Ubiquitin-binding domains in Y-family polymerases regulate translesion synthesis. Science *310*, 1821–1824.

Brotcorne-Lannoye, A., and Maenhaut-Michel, G. (1986). Role of RecA protein in untargeted UV mutagenesis of bacteriophage λ: evidence for the requirement for the dinB gene. Proc. Natl. Acad. Sci. USA *83*, 3904–3908.

Ducoux, M., Urbach, S., Baldacci, G., Hubscher, U., Koundrioukoff, S., Christensen, J., and Hughes, P. (2001). Mediation of proliferating cell nuclear antigen (PCNA)-dependent DNA replication through a conserved p21(Cip1)-like PCNA-binding motif present in the third subunit of human DNA polymerase δ. J. Biol. Chem. *276*, 49258–49266.

Fousteri, M., Vermeulen, W., van Zeeland, A.A., and Mullenders, L.H. (2006). Cockayne syndrome A and B proteins differentially regulate recruitment of chromatin remodeling and repair factors to stalled RNA polymerase II in vivo. Mol. Cell *23*, 471–482.

Friedberg, E.C., Lehmann, A.R., and Fuchs, R.P. (2005a). Trading places: how do DNA polymerases switch during translesion DNA synthesis? Mol. Cell *18*, 499–505.

Friedberg, E.C., Walker, G.C., Siede, W., Wood, R.D., Schultz, R.A., and Ellenberger, T. (2005b). DNA Repair and Mutagenesis, Second Edition (Washington, DC: ASM Press).

Gerik, K.J., Li, X., Pautz, A., and Burgers, P.M. (1998). Characterization of the two small subunits of Saccharomyces cerevisiae DNA polymerase δ. J. Biol. Chem. *273*, 19747–19755.

Gibbs, P.E., McDonald, J., Woodgate, R., and Lawrence, C.W. (2005). The relative roles in vivo of Saccharomyces cerevisiae Pol η, Pol ζ, Rev1 protein and Pol32 in the bypass and mutation induction of an abasic site, T-T (6-4) photoadduct and T-T cis-syn cyclobutane dimer. Genetics *169*, 575–582.

Gillet, L.C., and Scharer, O.D. (2006). Molecular mechanisms of mammalian global genome nucleotide excision repair. Chem. Rev. *106*, 253–276.

Guo, C., Tang, T.S., Bienko, M., Dikic, I., and Friedberg, E.C. (2008). Requirements for the interaction of mouse Polκ with ubiquitin and its biological significance. J. Biol. Chem. *283*, 4658–4664.

Hanawalt, P.C., and Spivak, G. (2008). Transcription-coupled DNA repair: two decades of progress and surprises. Nat. Rev. Mol. Cell Biol. *9*, 958–970.

Hanna, J.S., Kroll, E.S., Lundblad, V., and Spencer, F.A. (2001). Saccharomyces cerevisiae CTF18 and CTF4 are required for sister chromatid cohesion. Mol. Cell. Biol. *21*, 3144–3158.

Hoege, C., Pfander, B., Moldovan, G.L., Pyrowolakis, G., and Jentsch, S. (2002). RAD6-dependent DNA repair is linked to modification of PCNA by ubiquitin and SUMO. Nature *419*, 135–141.

Hughes, P., Tratner, I., Ducoux, M., Piard, K., and Baldacci, G. (1999). Isolation and identification of the third subunit of mammalian DNA polymerase delta by PCNA-affinity chromatography of mouse FM3A cell extracts. Nucleic Acids Res. *27*, 2108–2114.

Johnson, A., and O'Donnell, M. (2005). Cellular DNA replicases: components and dynamics at the replication fork. Annu. Rev. Biochem. *74*, 283–315.

Kai, M., and Wang, T.S. (2003). Checkpoint activation regulates mutagenic translesion synthesis. Genes Dev. *17*, 64–76.

Kannouche, P.L., Wing, J., and Lehmann, A.R. (2004). Interaction of human DNA polymerase η with monoubiquitinated PCNA: a possible mechanism for the polymerase switch in response to DNA damage. Mol. Cell *14*, 491–500.

Lam, L.H., and Reynolds, R.J. (1986). A sensitive, enzymatic assay for the detection of closely opposed cyclobutyl pyrimidine dimers induced in human diploid fibroblasts. Mutat. Res. *166*, 187–198.

Lee, M.Y., Jiang, Y.Q., Zhang, S.J., and Toomey, N.L. (1991). Characterization of human DNA polymerase δ and its immunochemical relationships with DNA polymerase α and ε. J. Biol. Chem. *266*, 2423–2429.

Lehmann, A.R. (2006). New functions for Y family polymerases. Mol. Cell *24*, 493–495.

Lehmann, A.R., Niimi, A., Ogi, T., Brown, S., Sabbioneda, S., Wing, J.F., Kannouche, P.L., and Green, C.M. (2007). Translesion synthesis: Y-family polymerases and the polymerase switch. DNA Repair (Amst.) *6*, 891–899.

Limsirichaikul, S., Niimi, A., Fawcett, H., Lehmann, A., Yamashita, S., and Ogi, T. (2009). A rapid non-radioactive technique for measurement of repair synthesis in primary human fibroblasts by incorporation of ethynyl deoxyuridine (EdU). Nucleic Acids Res. *37*, e31.

Majka, J., and Burgers, P.M. (2004). The PCNA-RFC families of DNA clamps and clamp loaders. Prog. Nucleic Acid Res. Mol. Biol. *78*, 227–260.

Masuda, Y., Suzuki, M., Piao, J., Gu, Y., Tsurimoto, T., and Kamiya, K. (2007). Dynamics of human replication factors in the elongation phase of DNA replication. Nucleic Acids Res. *35*, 6904–6916.

McCulloch, S.D., and Kunkel, T.A. (2008). The fidelity of DNA synthesis by eukaryotic replicative and translesion synthesis polymerases. Cell Res. *18*, 148–161.

Moldovan, G.L., Pfander, B., and Jentsch, S. (2007). PCNA, the maestro of the replication fork. Cell *129*, 665–679.

Moser, J., Kool, H., Giakzidis, I., Caldecott, K., Mullenders, L.H., and Fousteri, M.I. (2007). Sealing of chromosomal DNA nicks during nucleotide excision repair requires XRCC1 and DNA ligase III α in a cell-cycle-specific manner. Mol. Cell *27*, 311–323.

Mullenders, L.H., van Kesteren-van Leeuwen, A.C., van Zeeland, A.A., and Natarajan, A.T. (1985). Analysis of the structure and spatial distribution of ultraviolet-induced DNA repair patches in human cells made in the presence of inhibitors of replicative synthesis. Biochim. Biophys. Acta *826*, 38–48.

Nakajima, S., Lan, L., Kanno, S., Usami, N., Kobayashi, K., Mori, M., Shiomi, T., and Yasui, A. (2006). Replication-dependent and -independent responses of RAD18 to DNA damage in human cells. J. Biol. Chem. *281*, 34687–34695.

Nishida, C., Reinhard, P., and Linn, S. (1988). DNA repair synthesis in human fibroblasts requires DNA polymerase δ. J. Biol. Chem. *263*, 501–510.

Ogi, T., and Lehmann, A.R. (2006). The Y-family DNA polymerase κ (pol κ) functions in mammalian nucleotide-excision repair. Nat. Cell Biol. *8*, 640–642.

Ogi, T., Kannouche, P., and Lehmann, A.R. (2005). Localisation of human Y-family DNA polymerase κ: relationship to PCNA foci. J. Cell Sci. *118*, 129–136.

Ogiwara, H., Ohuchi, T., Ui, A., Tada, S., Enomoto, T., and Seki, M. (2007). Ctf18 is required for homologous recombination-mediated double-strand break repair. Nucleic Acids Res. *35*, 4989–5000.

Ohashi, E., Bebenek, K., Matsuda, T., Feaver, W.J., Gerlach, V.L., Friedberg, E.C., Ohmori, H., and Kunkel, T.A. (2000a). Fidelity and processivity of DNA synthesis by DNA polymerase κ, the product of the human DINB1 gene. J. Biol. Chem. *275*, 39678–39684.

Ohashi, E., Ogi, T., Kusumoto, R., Iwai, S., Masutani, C., Hanaoka, F., and Ohmori, H. (2000b). Error-prone bypass of certain DNA lesions by the human DNA polymerase κ. Genes Dev. *14*, 1589–1594.

Ohmori, H., Friedberg, E.C., Fuchs, R.P., Goodman, M.F., Hanaoka, F., Hinkle, D., Kunkel, T.A., Lawrence, C.W., Livneh, Z., Nohmi, T., et al. (2001). The Y-family of DNA polymerases. Mol. Cell *8*, 7–8.

Plosky, B.S., Vidal, A.E., Fernandez de Henestrosa, A.R., McLenigan, M.P., McDonald, J.P., Mead, S., and Woodgate, R. (2006). Controlling the subcellular localization of DNA polymerases ι and η via interactions with ubiquitin. EMBO J. *25*, 2847–2855.

Podust, V.N., Chang, L.S., Ott, R., Dianov, G.L., and Fanning, E. (2002). Reconstitution of human DNA polymerase δ using recombinant baculoviruses: the p12 subunit potentiates DNA polymerizing activity of the four-subunit enzyme. J. Biol. Chem. *277*, 3894–3901.

Prakash, S., Johnson, R.E., and Prakash, L. (2005). Eukaryotic translesion synthesis DNA polymerases: specificity of structure and function. Annu. Rev. Biochem. *74*, 317–353.

Shikata, K., Ohta, S., Yamada, K., Obuse, C., Yoshikawa, H., and Tsurimoto, T. (2001). The human homologue of fission Yeast cdc27, p66, is a component of active human DNA polymerase δ. J. Biochem. *129*, 699–708.

Shiomi, Y., Masutani, C., Hanaoka, F., Kimura, H., and Tsurimoto, T. (2007). A second proliferating cell nuclear antigen loader complex, Ctf18-replication factor C, stimulates DNA polymerase η activity. J. Biol. Chem. *282*, 20906–20914.

Smith, C.A., and Okumoto, D.S. (1984). Nature of DNA repair synthesis resistant to inhibitors of polymerase α in human cells. Biochemistry *23*, 1383–1391.

Staresincic, L., Fagbemi, A.F., Enzlin, J.H., Gourdin, A.M., Wijgers, N., Dunand-Sauthier, I., Giglia-Mari, G., Clarkson, S.G., Vermeulen, W., and Scharer, O.D. (2009). Coordination of dual incision and repair synthesis in human nucleotide excision repair. EMBO J. *28*, 1111–1120.

Suzuki, N., Ohashi, E., Kolbanovskiy, A., Geacintov, N.E., Grollman, A.P., Ohmori, H., and Shibutani, S. (2002). Translesion synthesis by human DNA polymerase κ on a DNA template containing a single stereoisomer of dG-(+)- or dG-(-)-anti-N^2-BPDE (7,8-dihydroxy-anti-9,10-epoxy-7,8,9,10-tetrahydrobenzo[*a*]pyrene). Biochemistry *41*, 6100–6106.

Volker, M., Mone, M.J., Karmakar, P., van Hoffen, A., Schul, W., Vermeulen, W., Hoeijmakers, J.H., van Driel, R., van Zeeland, A.A., and Mullenders, L.H.

(2001). Sequential assembly of the nucleotide excision repair factors in vivo. Mol. Cell *8*, 213–224.

Watanabe, K., Tateishi, S., Kawasuji, M., Tsurimoto, T., Inoue, H., and Yamaizumi, M. (2004). Rad18 guides poleta to replication stalling sites through physical interaction and PCNA monoubiquitination. EMBO J. *23*, 3886–3896.

Wood, R.D., and Shivji, M.K. (1997). Which DNA polymerases are used for DNA-repair in eukaryotes? Carcinogenesis *18*, 605–610.

Zhang, Y., Yuan, F., Xin, H., Wu, X., Rajpal, D.K., Yang, D., and Wang, Z. (2000). Human DNA polymerase κ synthesizes DNA with extraordinarily low fidelity. Nucleic Acids Res. *28*, 4147–4156.

Zhou, J.Q., He, H., Tan, C.K., Downey, K.M., and So, A.G. (1997). The small subunit is required for functional interaction of DNA polymerase δ with the proliferating cell nuclear antigen. Nucleic Acids Res. *25*, 1094–1099.

Osteoarthritis and Cartilage xxx (2010) 1–6

Osteoarthritis and Cartilage

OARSI OSTEOARTHRITIS RESEARCH SOCIETY INTERNATIONAL

In vivo structural analysis of subchondral trabecular bone in osteoarthritis of the hip using multi-detector row CT

K. Chiba †*, M. Ito ‡, M. Osaki †, M. Uetani ‡, H. Shindo †

† *Department of Orthopaedic Surgery, Nagasaki University School of Medicine, Japan*
‡ *Department of Radiology, Nagasaki University School of Medicine, Japan*

ARTICLE INFO

Article history:
Received 9 April 2010
Accepted 7 November 2010

Keywords:
Osteoarthritis of the hip
Subchondral trabecular bone
Microstructure
Computed tomography (CT)

SUMMARY

Objective: With developments in clinical computed tomography (CT), *in vivo* analysis of patients' bone microstructure has become increasingly possible. We analyzed the subchondral trabecular bone of hip osteoarthritis (OA) patients using multi-detector row CT (MDCT) to closely examine the structural changes that occur as OA progresses.

Design: 47 female hip joints were studied: 20 with OA secondary to hip dysplasia (11 advanced OA, nine early-moderate OA), seven with hip dysplasia without OA, and 20 normal. The images' maximal spatial resolution was 280 × 280 × 500 μm. Regions of interest (ROIs) were the subchondral trabecular bones of the acetabulum and femoral head. Measurement parameters were bone volume fraction (BV/TV), trabecular thickness (Tb.Th), trabecular number (Tb.N), trabecular separation (Tb.Sp), structure model index (SMI), trabecular bone pattern factor (TBPf), Euler's number, and degree of anisotropy (DA). Relationships between joint space volume and these parameters were analyzed.

Results: With decreasing joint space, Tb.Th and BV/TV increased, and Tb.Sp, Tb.N, SMI, TBPf, and DA decreased significantly. The microstructures were significantly different between the early to advanced OA groups and the normal and dysplasia groups; there was no significant difference between the normal and dysplasia groups.

Conclusions: Changes of subchondral trabecular bone structure in OA could be evaluated using MDCT, despite imperfect spatial resolution and limited accuracy. Trabecular bone thickening and associated structural changes may be closely related to OA. Changes were observed in early to advanced OA, but not in dysplasia. This method may help to further elucidate OA pathogenesis, determine the therapeutic strategy, and evaluate therapy.

Introduction

Osteoarthritis (OA) is a disease characterized by cartilage attrition and joint pain. The importance of subchondral bone in the etiology of OA has long been understood. The subchondral bone of OA exhibits various changes, such as trabecular bone thickening, cyst formation, decreased bone mineralization, and increased bone turn-over[1]. Trabecular bone thickening leads to bone sclerosis, which in turn causes decreased shock absorbency and cartilage damage[2]. High bone turn-over increases the release of various cytokines from subchondral bone, which can lead to cartilage degeneration. In OA animal models, subchondral bone resorption increases in the early stage. By using bone resorption inhibitor drugs, prevention of cartilage attrition has been reported[3]. In other words, subchondral bone and cartilage influence each other strongly, and subchondral bone changes in OA are not only the result of cartilage attrition, but also the cause of cartilage attrition.

The cartilage has no nerve supply, and one of the main causes of pain in OA is thought to be bone pain. The bone marrow lesion seen in OA subchondral bone on magnetic resonance imaging (MRI) is associated with microfractures, and a strong relationship with OA pain has been reported[4].

Disease-modifying OA drugs (DMOADs) are drugs aimed at fundamental treatment of OA; they are expected to become a mainstay of treatment for OA in the future. The target tissue includes the subchondral bone, in addition to the articular cartilage and synovium. In other words, by early detection of OA and by normalization of bone metabolism and bone structure, OA progression and symptoms may be preventable. Candidate drugs currently reported include alendronate, risedronate, and calcitonin[3,5,6]. Osteotomy also improves OA progression and symptoms

* Address correspondence and reprint requests to: K. Chiba, 1-7-1 Sakamoto, Nagasaki 852-8501, Japan. Tel: 81-95-819-7321; Fax: 81-95-849-7325.
E-mail address: kohchiba@estate.ocn.ne.jp (K. Chiba).

1063-4584/$ – see front matter © 2010 Osteoarthritis Research Society International. Published by Elsevier Ltd. All rights reserved.
doi:10.1016/j.joca.2010.11.002

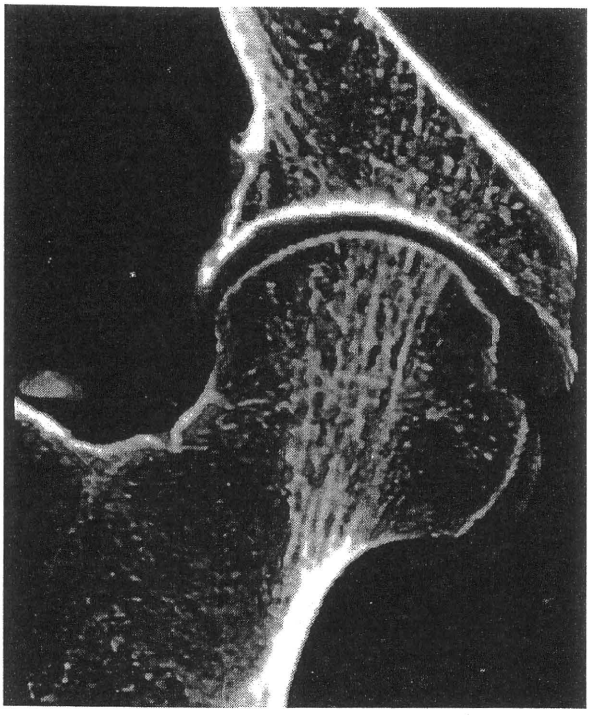

Fig. 1. 3D reconstructed MDCT image of a normal hip joint. The principal compressive trabeculae of the femoral head and corresponding acetabular trabeculae are well demonstrated, although the others are not clear because of insufficient spatial resolution.

by altering the mechanical environment of the joint. After the surgery, normalization of trabecular structure, such as decreased bone sclerosis and a reduction in bone cysts, has been observed.

Therefore, evaluation of subchondral bone, in addition to cartilage, by clinical imaging techniques is very important in analyzing the etiology of OA and assessing treatment in patients.

Generally, analysis of bone microstructure has been performed by pathological examination or micro computed tomography (CT), which basically provides *in vitro* analysis only for the extracted bone samples. However, owing to the remarkable development of clinical medical imaging such as CT and MRI in recent years, it is possible to analyze patients' bone microstructure *in vivo*. Multi-detector row CT (MDCT), which has become widespread and is able to scan thin slice images in a short time, provides higher resolution images than before. Several studies have shown the usefulness of *in vivo* bone microstructure analysis by MDCT in osteoporosis cases[7,8].

In this study, a cross-sectional analysis of the subchondral trabecular bone microstructure of patients with hip OA using clinical MDCT was conducted to answer the following research questions: whether changes in trabecular bone structure in hip OA can be evaluated with clinical CT; what kinds of changes are most pronounced; and when and where those changes occur.

Methods

Subjects

Twenty female patients with hip OA secondary to hip dysplasia and 20 female normal volunteers were investigated from 2007 to 2008. The hip OA patients had undergone CT examination for hip OA surgery. Patients with hip OA secondary to avascular necrosis, rheumatoid arthritis, or trauma and those with a history of osteotomy or contralateral arthroplasty were excluded. The normal volunteers had undergone health checks at our hospital and volunteered to participate in this study. They were interviewed and underwent CT examinations, after which those who had hip joint disease or were taking medications that could affect bone metabolism were excluded. The analysis included 47 hip joints: 11 hip joints were advanced OA (Tönnis grade 3), nine were early to moderate OA (grade 1–2), seven were hip dysplasia without OA, and 20 were normal hips[9]. Hip joints on the unaffected side in OA patients were excluded from the analysis. In the normal volunteers, only the left hip was analyzed.

The mean age was 69 ± 6 (range 59–81) years for advanced OA, 66 ± 10 (45–81) years for early-moderate OA, 63 ± 9 (49–74) years for hip dysplasia without OA, and 66 ± 9 (50–80) years for normal volunteers ($P = 0.412$). The center-edge (CE) angle was 19 ± 12 (2–43)° in the advanced group, 12 ± 13 (−17–28)° in the early-moderate group, 12 ± 8 (0–20)° in the dysplasia group, and 36 ± 5 (27–44)° in the normal group. The CE angle is formed by a line from the center of the femoral head to the lateral edge of the acetabular roof and a vertical line drawn through the center of the femoral head[10]. The acetabular angle was 43 ± 4 (34–50)° in the advanced group, 43 ± 4 (38–48)° in the early-moderate group, 47 ± 4

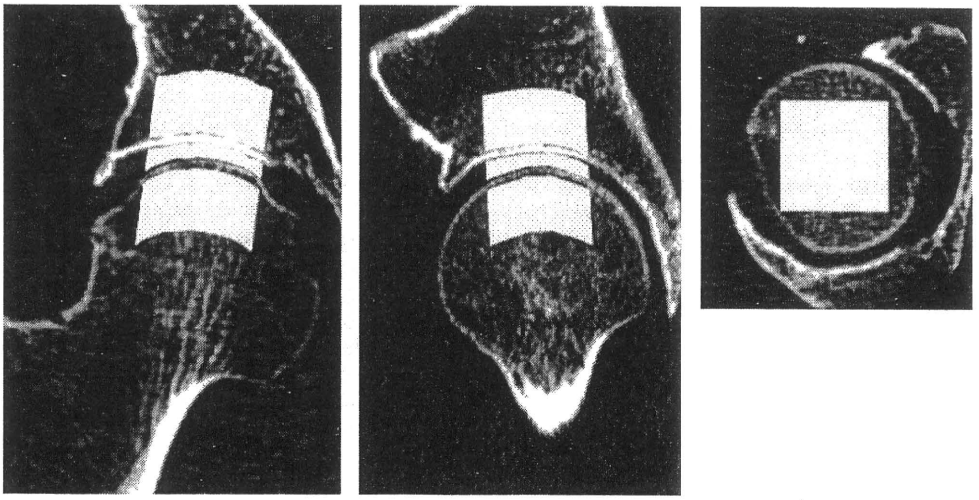

Fig. 2. ROI for the bone microstructure analysis. The subchondral trabecular bone structure of the acetabulum and femoral head and the joint space volume were measured. The subchondral bone region is a 2 × 2 cm^2 area, 1 cm under the subchondral endplate, and aligned with the principal compressive trabeculae.

Please cite this article in press as: Chiba K, et al., *In vivo* structural analysis of subchondral trabecular bone in..., Osteoarthritis and Cartilage (2010), doi:10.1016/j.joca.2010.11.002

Table I
Relationship between joint space volume and subchondral bone microstructure

	Joint space volume vs acetabular bone structure		Joint space volume vs femoral head bone structure	
	r	P	r	P
App BV/TV	−0.691	<0.001	−0.729	<0.001
App Tb.Th	−0.628	<0.001	−0.665	<0.001
App Tb.N	0.205	Ns	0.435	<0.01
App Tb.Sp	0.41	<0.01	0.192	Ns
SMI	0.651	<0.001	0.558	<0.001
TBPf	0.726	<0.001	0.666	<0.001
Euler's N	−0.187	Ns	−0.369	<0.05
DA	0.468	<0.001	−0.076	Ns

(43–55)° in the dysplasia group, and 39 ± 2 (35–43)° in the normal group. The acetabular angle is formed by a horizontal line connecting both tear drops and a line from a tear drop to the lateral edge of the acetabular roof[11]. The study protocol was approved by the ethics review board of our institute and complied with the Declaration of Helsinki of 1975, revised in 2000.

CT scanning

An MDCT with 16 detectors (Aquilion 16, Toshiba, Tokyo, Japan) was used. Scanning was performed at 120 kV, 300 mAs, and 0.5-mm thickness. Images were reconstructed with a field of view (FOV) of 70 mm, 512 × 512 pixel matrix, and 0.2-mm pitch (Fig. 1). The maximal in-plane resolution was 280 × 280 μm^2, and the axial resolution was 500 μm, based on the manufacturer's data. CTDIvol was 19.7 mGy, and DLP was 331 mGy, which were almost the same as for conventional abdominal CT scans.

Microstructure analysis

The microstructure of subchondral trabecular bone was measured by bone structure measurement software (TRI/3D-BON, Ratoc System Engineering Co., Tokyo, Japan). CT images were reconstructed to coronal images for bone structure analysis to facilitate differentiation between cartilage and subchondral bone. Regions of interest (ROIs) were subchondral trabecular bones of the acetabulum and femoral head, 1 cm under the subchondral endplate, 2 × 2 cm^2 area, and aligned with the principal compressive trabeculae of the femoral head (Fig. 2). The bone cyst region was strictly excluded from the ROIs. The joint space volume aligned with the ROI was also measured. ROI was established semi-automatically by a single orthopedist. Square columns of 2 × 2 cm^2 were set manually, and cartilage was manually corrected after being automatically extracted. Using the magnification function, a region 1 cm from the subchondral endplate was specified. The binarization was performed using a fixed threshold value, which was calculated by a discriminant analysis between the bone and the background in the histogram. Threshold values were obtained from eight normal volunteers' femoral head trabecular bone areas, and their mean was defined as the fixed threshold value.

The measurement parameters were apparent bone volume fraction (BV/TV), apparent trabecular thickness (app Tb.Th), apparent trabecular number (app Tb.N), apparent trabecular separation (app Tb.Sp), structure model index (SMI), trabecular bone pattern factor (TBPf), Euler's number, and degree of anisotropy (DA)[12–15]. SMI is an index evaluating whether trabecular bone is rod-like or plate-like, and a small value means a more plate-like structure. TBPf is also an index evaluating rod-like, plate-like, or honeycomb-like structure, and a small value means a more honeycomb-like structure. Euler's number represents the connectivity of trabecular bone, and a small value means a more connected structure. In trabecular bone converted to a linear drawing, this was defined as Euler number = number of trabecular bone components − number of through holes + number of cavities. Connectivity is higher when there is a greater number of through holes. DA was determined from the ratio between the maximal and minimal radii of the mean intercept length (MIL) ellipsoid. The mean length of lines cut by lines parallel to an arbitrary angle is called the MIL. When plotted on polar coordinates, this resembles an ellipsoid, which is called an MIL ellipsoid. By taking the ratio of the long and short axes of the ellipsoid, anisotropy can be quantified.

The reproducibility of the measurements was estimated by calculating the intra-class correlation coefficient (ICC) of three investigators' measurements of three randomly chosen CT studies three times. Intra-tester reproducibility and inter-tester reproducibility were: 0.64 and 0.66, respectively, for BV/TV; 0.97 and 0.97, respectively, for Tb.Th; 0.99 and 0.99, respectively, for Tb.N; 0.98 and 0.97, respectively, for Tb.Sp; 0.99 and 0.99, respectively, for SMI; 0.97 and 0.97, respectively, for TBPf; 0.99 and 0.99, respectively, for Euler's number; and 0.99 and 0.99, respectively, for DA.

Statistical analysis

The relationships between joint space volume, CE angle, acetabular angle, and these microstructure parameters were analyzed by Pearson's correlation test. Differences in these microstructure parameters among the normal, dysplasia, early-moderate OA, and advanced OA groups were analyzed using the Bonferroni test (SPSS 16.0, Chicago, IL, USA). $P < 0.05$ was considered statistically significant.

Results

As the joint space narrowed, trabecular bone thickened, bone volume fraction increased, and the trabecular morphology became

Table II
Relationship between acetabular dysplasia and subchondral bone microstructure

	CE angle vs acetabular bone structure		CE angle vs femoral head bone structure		Acetabular angle vs acetabular bone structure		Acetabular angle vs femoral head bone structure	
	r	P	r	P	r	P	r	P
App BV/TV	−0.617	<0.001	−0.429	<0.01	0.393	<0.01	0.257	Ns
App Tb.Th	−0.554	<0.001	−0.369	<0.05	0.280	Ns	0.139	Ns
App Tb.N	−0.115	Ns	0.221	Ns	0.154	Ns	−0.152	Ns
App Tb.Sp	0.328	<0.05	0.089	Ns	−0.149	Ns	−0.136	Ns
SMI	0.294	<0.05	0.291	<0.05	−0.382	<0.01	−0.230	Ns
TBPf	0.530	<0.001	0.404	<0.01	−0.392	<0.01	−0.286	Ns
Eider's N	−0.142	Ns	−0.165	Ns	−0.055	Ns	0.125	Ns
DA	02.07	Ns	−0.509	<0.001	−0.196	Ns	0.272	Ns

Please cite this article in press as: Chiba K, et al., *In vivo* structural analysis of subchondral trabecular bone in..., Osteoarthritis and Cartilage (2010), doi:10.1016/j.joca.2010.11.002

Table III
Acetabular subchondral bone microstructure of each group (Mean, 95% CI)

	Normal	Dysplasia	Early-moderate OA	Advanced OA
App BV/TV (%)	29.8 (26.1, 33.5)	31.8 (23.6, 39.9)	59.1‡, ¶ (45.2, 72.9)	73.1‡, ¶ (62.0, 84.2)
App Tb.Th (μm)	1018 (930, 1106)	1143 (1011, 1276)	1520† (1212, 1829)	1909‡, ¶ (1563, 2255)
App Tb.N (1/mm)	0.14 (0.13, 0.16)	0.14 (0.11, 0.17)	0.15 (0.13, 0.17)	0.13 (0.11, 0.15)
App Tb.Sp (μm)	1111 (1037, 1185)	1259 (953, 1565)	839§ (590, 1089)	887§ (657, 1118)
SMI	2.31 (2.16, 2.46)	2.29 (1.74, 2.84)	1.77 (1.13, 2.40)	0.89‡, ¶, # (0.28, 1.51)
TBPf (1/mm)	1.11 (0.90, 1.31)	0.97 (0.46, 1.48)	−0.09‡, ‖ (−0.52, 0.34)	−0.72‡, ¶ (−1.14, −0.30)
Euler's N	−100 (−131, −69)	−76 (−165, 13)	−81 (−126, −35)	−57 (−104, −11)
DA	2.42 (2.13, 2.72)	2.52 (1.26, 3.79)	1.78 (1.51, 2.05)	1.63* (1.50, 1.77)

* vs Normal $P < 0.05$.
† vs Normal $P < 0.01$.
‡ vs Normal $P < 0.001$.
§ vs Dysplasia $P < 0.05$.
‖ vs Dysplasia $P < 0.01$.
¶ vs Dysplasia $P < 0.001$.
# vs Early-Moderate OA $P < 0.05$.

more plate-like and honeycomb-like on both the acetabular and femoral head sides. In addition, on the acetabular side, the distance between bone trabeculae lessened, and anisotropy decreased as the joint space narrowed. On the femoral head side, there were fewer bone trabeculae and decreased connectivity as the joint space narrowed (Table I). The same tendencies were also seen in the relation between the CE angle and trabecular bone structure, but the correlation coefficient with the acetabular angle was small (Table II).

These changes were significant from early-moderate OA on the acetabular side, and they occurred prominently in advanced OA (Table III). On the femoral head side, changes in number, though not significant, appeared in early-moderate OA. Then, in advanced OA, they were significant (Table IV).

Figure 3 is the scattergram of the joint space volume and app Tb.Th of the femoral head subchondral bone. They had a negative correlation ($r = -0.665$, $P < 0.001$), and the app Tb.Th increased in early to advanced OA, but not in dysplasia. Figure 4 shows the 3D reconstructed MDCT images of subchondral trabecular bone of normal and advanced OA cases. The subchondral trabecular bone of the advanced OA patient shows thickening and union of trabecular bones.

Discussion

To the best of our knowledge, there has been no previously reported *in vivo* analysis of the subchondral bone microstructure of patients with hip dysplasia and OA using clinical MDCT. So far, *in vivo* analysis of human trabecular bone by clinical MDCT has been performed mainly for the evaluation of osteoporosis. Ito *et al.* evaluated vertebral microstructure and fracture risk using MDCT, showing superior predictive ability than dual X-ray absorptiometry[7]. Graeff *et al.* also studied vertebral microstructure by MDCT and monitored drug-associated changes[8].

In recent years, several studies have shown the possibility of *in vivo* analysis of human hip joints by clinical MDCT. Bauer *et al.* analyzed the trabecular structure of bone samples from the femoral head by MDCT in a simulated soft-tissue environment; they concluded that the major characteristics of the trabecular network could still be appreciated and quantified, even though soft-tissue scatter substantially compromises image quality[16]. Diederichs *et al.* also showed the feasibility of measuring trabecular bone structure of the proximal femur using MDCT in a clinical setting[17].

In this study, we found that, as the joint space volume decreased, Tb.Th and bone volume fraction increased. This is thought to be due to adaptation to increased loading on the joint or thickening as a repair mechanism when microfractures develop. Thickening of trabeculae would induce a decrease in Tb.Sp at the acetabular subchondral bone. (Table I). On the other hand, the Tb.Th increased, but Tb.N decreased at the femoral head subchondral bone, which might mean that trabecular thickening caused a union of trabecular bones, resulting in decreased Tb.N. The union of trabecular bone was probably related to both true trabecular thickening and a partial volume effect (Table I, Fig. 4). SMI and TBPf at both subchondral bone locations decreased as the joint space volume decreased. Thickening of trabecular bone would also cause more plate-like and

Table IV
Femoral head subchondral bone microstructure of each group (Mean, 95% CI)

	Normal	Dysplasia	Early-moderate OA	Advanced OA
App BV/TV (%)	30.2 (24.4, 35.9)	28.5 (17.5, 39.4)	45.6 (30.1, 61.0)	68.5‡, ¶, ††(59.2, 77.9)
App Tb.Th (μm)	803 (749, 856)	804 (704, 903)	1240(811, 1668)	1773‡, ¶, # (1.336, 2209)
App Tb.N (1/mm)	0.21 (0.19, 0.24)	0.21 (0.15, 0.27)	0.18 (0.14, 0.23)	0.13†, § (0.10, 0.16)
App Tb.Sp (μm)	830 (752, 908)	888 (629, 1146)	803 (645, 961)	746 (586, 906)
SMI	2.03 (1.68, 2.37)	2.09 (1.50, 2.68)	1.59 (0.69, 2.49)	0.66% (−0.17, 1.49)
TBPf (1/mm)	1.08 (0.71, 1.45)	1.13 (0.39, 1.88)	0.29 (−0.141, 1.00)	−0.59‡, ¶ (−0.94, −0.23)
Euler's N	−270 (−359, −181)	−247 (−418, −76)	−187 (−306, −68)	−89* (−139, −39)
DA	1.32 (1.23, 1.42)	1.59* (1.42, 1.75)	1.57* (1.37, 1.77)	1.51 (1.40, 1.62)

* vs Normal $P < 0.05$.
† vs Normal $P < 0.01$.
‡ vs Normal $P < 0.001$.
§ vs Dysplasia $P < 0.05$.
‖ vs Dysplasia $P < 0.01$.
¶ vs Dysplasia $P < 0.001$.
# vs Early-Moderate OA $P < 0.05$.
†† vs Early-Moderate OA $P < 0.01$.

Please cite this article in press as: Chiba K, et al., *In vivo* structural analysis of subchondral trabecular bone in..., Osteoarthritis and Cartilage (2010), doi:10.1016/j.joca.2010.11.002

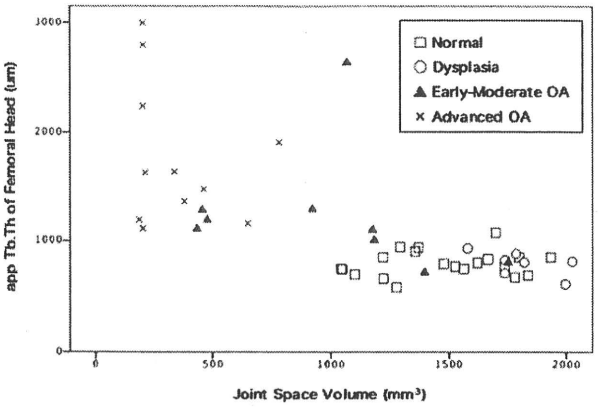

Fig. 3. Relationship between joint space volume and app Tb.Th of femoral head subchondral bone. There is a negative correlation between joint space volume and app Tb.Th. ($r = -0.665$, $P < 0.001$). App Tb.Th increases in early and advanced staged OA, but not in dysplasia.

honeycomb-like structures of the trabecular bones. DA at the acetabular subchondral bone decreased as the joint space volume decreased. Low bone volume fraction bone generally has high anisotropy to preserve only trabecular bone for weight bearing. Therefore, decreased joint space and the subsequent high bone volume fraction might decrease DA. Correlation coefficients were high for bone volume fraction, Tb.Th, and TBPf, suggesting that these parameters were sensitive for the evaluation of OA.

Chappard *et al.* performed a detailed study of the subchondral bone microstructure of hip OA using synchrotron micro CT. They found that the OA subchondral bone had increased bone volume fraction and Tb.Th, and decreased Tb.Sp[1]. Ding *et al.* also investigated the features of subchondral bone of knee OA using conventional micro CT and showed increased bone volume fraction and Tb.Th, and decreased SMI[18]. These results are similar to ours. Therefore, although accuracy was limited, change of the subchondral trabecular bone structure in OA could be evaluated by MDCT to a certain extent.

These changes were observed in early to advanced OA, but not in dysplasia (Tables III and IV). Dysplasia alone might not cause subchondral bone changes, or small changes could not be detected because of the lack of spatial resolution. In the early-moderate OA group, significant changes were observed only at acetabular subchondral bone (Tables III and IV). The data suggest that OA changes in subchondral trabecular bone might occur predominantly at the acetabular side rather than the femoral head side.

Generally it is difficult to analyze bone microstructure of dysplasia and early OA patients by micro CT, because these bone samples are not easily available. Arthroplasty is usually performed for advanced OA patients, and it is hard to extract subchondral bone samples from the acetabular side. Furthermore, finding cadavers with dysplasia and early OA is not easy. Therefore, information regarding the bone microstructure of dysplasia and of early OA patients is valuable.

In the future, the therapeutic approach to OA will shift to early detection, prognosis prediction, and preventive therapy. This method may play a useful role in all these steps. Using this method, we could predict which OA patients would develop destructive changes, with atrophic and collapse changes. Furthermore, we could use this method to determine whether osteotomy and DMOADs were indicated, and evaluate the effects of these treatments. This study could be a first step in realizing these potential uses.

The limitation of this study was limited accuracy. The spatial resolution of this method was $500 \times 280 \times 280\ \mu m^3$, which is basically insufficient to allow perfect visualization of trabecular bone. It causes a partial volume effect; several trabecular bones unite with each other and look like one large trabecular bone, and small trabecular bone cannot be detected and vanishes, looking like there is no bone (Fig. 1). In addition, there is more noise in clinical CT images than in experimental images because of soft tissues and patient movement[16,17]. Our group has already reported an *in vivo* analysis of trabecular bone microstructure using MDCT, which had a spatial resolution of $500 \times 210 \times 210\ \mu m^3$ that was similar to that in the present study. In this report, we confirmed the validity of the accuracy of this method by comparing the MDCT images with the micro CT images[7]. Other papers also suggest the possibility of *in vivo* microstructure analysis of the hip joint by MDCT[16,17]. Advances in MDCT continue to be made, and the spatial resolution is increasing, with less noise and lower radiation doses. These advances will likely lead to fewer accuracy problems in the future.

This study was a cross-sectional study, and a longitudinal study might show earlier changes of OA subchondral trabecular bone. Strictly speaking, the joint space volume is not equal to the cartilage volume. However, we think that the gap between the acetabular and femoral cartilages would be so small that such error is acceptable.

In conclusion, we have shown the possibility of evaluating trabecular structure in hip OA patients using clinical CT. Increased trabecular bone width and accompanying structural changes may be closely related to OA. These changes do not appear in the stage with dysplasia only, but they appear when the condition reaches early-moderate OA, predominantly on the acetabular side. This method may be applied to further elucidate the pathogenesis of OA, to decide the therapeutic strategy, and to evaluate the effects of treatment.

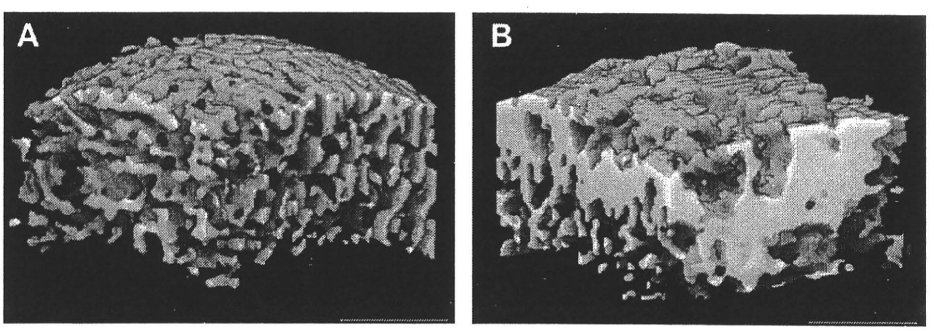

Fig. 4. 3D reconstructed MDCT images of femoral head subchondral trabecular bone of a normal subject (A) and an advanced OA patient (B). The subchondral trabecular bone of the OA patient shows mass formation by thick trabecular bones.

Please cite this article in press as: Chiba K, et al., *In vivo* structural analysis of subchondral trabecular bone in..., Osteoarthritis and Cartilage (2010), doi:10.1016/j.joca.2010.11.002

Author contributions

KC: design, collection and analysis of data, and drafting of the article. MI: design, collection and analysis of data, revision of the article. MO, MU, and HS: design, collection of data, and revision of the article. Masako Ito, masako@nagasaki-u.ac.jp.

Role of the funding source

This research was partially supported by a Grant-in-Aid for Scientific Research for Young Researchers (B) by the Japan Society for the Promotion of Science (JSPS).

Conflict of interest

No competing interests declared.

Acknowledgments

The authors would like to thank Toru Fukuda and Tomoko Nakata (Division of Radiology, Nagasaki University Hospital, Nagasaki, Japan) for CT scanning.

References

1. Chappard C, Peyrin F, Bonnassie A, Lemineur G, Brunet-Imbault B, Lespessailles E, *et al.* Subchondral bone micro-architectural alterations in osteoarthritis: a synchrotron micro-computed tomography study. Osteoarthritis Cartilage 2006;14:215–23.
2. Radin EL, Rose RM. Role of subchondral bone in the initiation and progression of cartilage damage. Clin Orthop Relat Res 1986;213:34–40.
3. Hayami T, Pickarski M, Wesolowski GA, McLane J, Bone A, Destefano J, *et al.* The role of subchondral bone remodeling in osteoarthritis: reduction of cartilage degeneration and prevention of osteophyte formation by alendronate in the rat anterior cruciate ligament transection model. Arthritis Rheum 2004;50:1193–206.
4. Felson DT, Niu J, Guermazi A, Roemer F, Aliabadi P, Clancy M, *et al.* Correlation of the development of knee pain with enlarging bone marrow lesions on magnetic resonance imaging. Arthritis Rheum 2007;56:2986–92.
5. Garnero P, Aronstein WS, Cohen SB, Conaghan PG, Cline GA, Christiansen C, *et al.* Relationships between biochemical markers of bone and cartilage degradation with radiological progression in patients with knee osteoarthritis receiving risedronate: the Knee Osteoarthritis Structural Arthritis randomized clinical trial. Osteoarthritis Cartilage 2008;16:660–6. Epub 2007 Nov 13.
6. Manicourt DH, Altman RD, Williams JM, Devogelaer JP, Druetz-Van Egeren A, Lenz ME, *et al.* Treatment with calcitonin suppresses the responses of bone, cartilage, and synovium in the early stages of canine experimental osteoarthritis and significantly reduces the severity of the cartilage lesions. Arthritis Rheum 1999;42:1159–67.
7. Ito M, Ikeda K, Nishiguchi M, Shindo H, Uetani M, Hosoi T, *et al.* Multi-detector row CT imaging of vertebral microstructure for evaluation of fracture risk. J Bone Miner Res 2005;20:1828–36.
8. Graeff C, Timm W, Nickelsen TN, Farrerons J, Marin F, Barker C, *et al.* Monitoring teriparatide-associated changes in vertebral microstructure by high-resolution CT in vivo: results from the EUROFORS study. J Bone Miner Res 2007;22:1426–33.
9. Tönnis D. Normal values of the hip joint for the evaluation of X-rays in children and adults. Clin Orthop Relat Res 1976;119:39–47.
10. Wiberg G. Studies on dysplastic acetabula and congenital subluxation of the hip joint. With special reference to the complication of osteoarthritis. Acta Chir Scand 1939;58:28–38.
11. Sharp IK. Acetabular dysplasia: the acetabular angle. J Bone Joint Surg Br 1961;43:268–72.
12. Odgaard A, Gundersen HJ. Quantification of connectivity in cancellous bone, with special emphasis on 3-D reconstructions. Bone 1993;14:173–82.
13. Hildebrand T, Rüegsegger P. Quantification of bone microarchitecture with the structure model index. Comput Methods Biomech Biomed Engin 1997;1:15–23.
14. Hahn M, Vogel M, Pompesius-Kempa M, Delling G. Trabecular bone pattern factor — a new parameter for simple quantification of bone microarchitecture. Bone 1992;13:327–30.
15. Harrigan TP, Mann RW. Characterization of microstructural anisotropy in orthotropic materials using a second rank tensor. J Mater Sci 1984;19:761–7.
16. Bauer JS, Link TM, Burghardt A, Henning TD, Mueller D, Majumdar S, *et al.* Analysis of trabecular bone structure with multidetector spiral computed tomography in a simulated soft-tissue environment. Calcif Tissue Int 2007;80:366–73.
17. Diederichs G, Link T, Marie K, Huber M, Rogalla P, Burghardt A, *et al.* Feasibility of measuring trabecular bone structure of the proximal femur using 64-slice multidetector computed tomography in a clinical setting. Calcif Tissue Int 2008;83:332–41.
18. Ding M, Odgaard A, Hvid I. Changes in the three-dimensional microstructure of human tibial cancellous bone in early osteoarthritis. J Bone Joint Surg Br 2003;85:906–12.

Please cite this article in press as: Chiba K, et al., *In vivo* structural analysis of subchondral trabecular bone in..., Osteoarthritis and Cartilage (2010), doi:10.1016/j.joca.2010.11.002

Bone xxx (2010) xxx–xxx

Contents lists available at ScienceDirect

Bone

journal homepage: www.elsevier.com/locate/bone

Age-related changes in bone density, geometry and biomechanical properties of the proximal femur: CT-based 3D hip structure analysis in normal postmenopausal women

Masako Ito [a,b,*], Tomoko Nakata [b], Akifumi Nishida [a], Masataka Uetani [a]

[a] Department of Radiology, Nagasaki University School of Medicine, 1-7-1 Sakamoto, Nagasaki 852-8501, Japan
[b] Division of Radiology, Nagasaki University Hospital, Nagasaki, Japan

ARTICLE INFO

Article history:
Received 24 September 2010
Revised 5 November 2010
Accepted 9 November 2010
Available online xxxx

Edited by: Toshio Matsumoto

Keywords:
Hip geometry
Bone mineral density (BMD)
Computed tomography (CT)
Osteoporosis

ABSTRACT

The geometry as well as bone mineral density (BMD) of the proximal femur contributes to fracture risk. How and the extent to which they change due to natural aging is not fully understood.

We assessed BMD and geometry in the femoral neck and shaft separately, in 59 normal Japanese postmenopausal women aged 54–84 years, using clinical computed tomography (CT) and commercially available software, at baseline and 2-year follow-up. This system detected significant reductions over the 2-year interval in total BMD (%change/year = -0.900 ± 0.257, $p<0.0005$), cortical cross-sectional area (CSA) (-0.800 ± 0.423%/year, $p<0.05$) and cortical thickness (-1.120 ± 0.453%/year, $p<0.01$) in the femoral neck. In the femoral shaft, cortical BMD decreased significantly (-0.642 ± 0.188%/year, $p<0.005$). Regarding biomechanical parameters in the femoral neck, the cross-sectional moment of inertia (CSMI) and section modulus (SM) decreased (-1.38 ± 3.65%/year, $p<0.01$ and -1.37 ± 2.96%/year, $p<0.005$) and the buckling ratio (BR) increased significantly (1.48 ± 4.81%/year, $p<0.05$), whereas no changes were found in the femoral shaft.

The distinct patterns of age-related changes in the geometry and biomechanical properties in the femoral neck and shaft suggest that improved geometric measures are possible with the current non-invasive method using clinical CT.

Introduction

The incidence of vertebral fracture increases linearly with aging and correlates closely with a decline in spinal bone mineral density (BMD). The incidence of hip fracture, on the other hand, increases exponentially with advancing age, although hip BMD decreases linearly, suggesting that age-related factors other than BMD contribute substantially to the fragility of the proximal femur. Declining BMD and geometry of the proximal femur, as well as an increase in the incidence of fall are believed to underlie the increased risk of hip fracture in the elderly [1–3]. Non-invasive techniques can provide bone structural information, beyond simple bone densitometry, to help assess fracture risk.

The aging skeleton is characterized by a deterioration of the trabecular microstructure, increased endocortical bone resorption, decreased cortical bone density or increased cortical porosity, and increased periosteal bone formation [4]. In postmenopausal women, the rate of periosteal bone formation declines to a greater extent, while endosteal bone resorption is more elevated, compared with age-matched men. However, the natural course of these cortical changes with aging has not been well elucidated, and how faithfully non-invasive methods can detect these changes over time is also unknown.

Age-related changes in the cortical bone of the femoral neck as well as the shaft have been investigated by means of histology or computed tomography (CT) images. Although cross-sectional analyses of age-related changes in hip geometry have been reported using clinical CT [5,6] or dual X-ray absortiometry (DXA) [7], there have been no reports of age-related changes in geometry along with BMD in the femoral neck and shaft simultaneously, and which also followed the changes longitudinally in the same subjects.

Here we report the results of longitudinal as well as cross-sectional analyses of clinical CT on age-related changes in BMD, geometry and biomechanical properties of the proximal femur, neck and shaft separately, in the same cohort of healthy postmenopausal Japanese women. The information provided in this study may form the basis for future investigation into how osteoporosis intervention impacts the biomechanical properties along with the structure of the femoral neck and shaft.

* Corresponding author. Department of Radiology, Nagasaki University School of Medicine, 1-7-1 Sakamoto, Nagasaki 852-8501, Japan. Fax: +81 95 819 7357.
E-mail address: masako@nagasaki-u.ac.jp (M. Ito).

8756-3282/$ – see front matter © 2010 Elsevier Inc. All rights reserved.
doi:10.1016/j.bone.2010.11.007